KOI-2700b—A PLANET CANDIDATE WITH DUSTY EFFLUENTS ON A 22 hr ORBIT

Citation: Rappaport, Saul, Thomas Barclay, John DeVore, Jason Rowe, Roberto Sanchis-Ojeda, and Martin Still. “KOI-2700b—A PLANET CANDIDATE WITH DUSTY EFFLUENTS ON A 22 Hr ORBIT.” The Astrophysical Journal 784, no. 1 (March 3, 2014): 40. © The American Astronomical Society

As Published: http://dx.doi.org/10.1088/0004-637x/784/1/40

Publisher: IOP Publishing

Persistent URL: http://hdl.handle.net/1721.1/93137

Version: Final published version: final published article, as it appeared in a journal, conference proceedings, or other formally published context

The Astrophysical Journal, 784:40 (16pp), 2014 March 20 doi:10.1088/0004-637X/784/1/40

KOI-2700b—A PLANET CANDIDATE WITH DUSTY EFFLUENTS ON A 22 hr ORBIT

Saul Rappaport[1], Thomas Barclay[2], John DeVore[3], Jason Rowe[4,5], Roberto Sanchis-Ojeda[1], and Martin Still[2]
[1] Department of Physics, and Kavli Institute for Astrophysics and Space Research, Massachusetts Institute of Technology,
Cambridge, MA 02139, USA; sar@mit.edu, rsanchis86@gmail.com
[2] BAER Institute/NASA Ames Research Center, M/S 244-30, Moffett Field, Mountain View, CA 94035, USA; thomas.barclay@nasa.gov, martin.d.still@nasa.gov
[3] Visidyne, Inc., 111 South Bedford St., Suite 103, Burlington, MA 01803, USA; devore@visidyne.com
[4] SETI Institute, 189 Bernardo Ave, Suite 100 Mountain View, CA 94043, USA
[5] NASA Ames Research Center, M/S 244-30, Moffett Field, Mountain View, CA 94035, USA; jasonfrowe@gmail.com

Received 2013 November 6; accepted 2014 January 26; published 2014 March 3

ABSTRACT

Kepler planet candidate KOI-2700b (KIC 8639908b), with an orbital period of 21.84 hr, exhibits a distinctly asymmetric transit profile, likely indicative of the emission of dusty effluents, and reminiscent of KIC 1255b. The host star has $T_{\rm eff} = 4435$ K, $M \simeq 0.63\,M_\odot$, and $R \simeq 0.57\,R_\odot$, comparable to the parameters ascribed to KIC 12557548. The transit egress can be followed for ∼25% of the orbital period and, if interpreted as extinction from a dusty comet-like tail, indicates a long lifetime for the dust grains of more than a day. We present a semiphysical model for the dust tail attenuation and fit for the physical parameters contained in that expression. The transit is not sufficiently deep to allow for a study of the transit-to-transit variations, as is the case for KIC 1255b; however, it is clear that the transit depth is slowly monotonically decreasing by a factor of ∼2 over the duration of the *Kepler* mission. We infer a mass-loss rate in dust from the planet of ∼2 lunar masses per Gyr. The existence of a second star hosting a planet with a dusty comet-like tail would help to show that such objects may be more common and less exotic than originally thought. According to current models, only quite small planets with $M_p \lesssim 0.03\,M_\oplus$ are likely to release a detectable quantity of dust. Thus, any "normal-looking" transit that is inferred to arise from a rocky planet of radius greater than $\sim 1/2\,R_\oplus$ should not exhibit any hint of a dusty tail. Conversely, if one detects an asymmetric transit due to a dusty tail, then it will be very difficult to detect the hard body of the planet within the transit because, by necessity, the planet must be quite small (i.e., $\lesssim 0.3\,R_\oplus$).

Key words: planetary systems – planets and satellites: detection – planets and satellites: individual (KOI-2700b)

Online-only material: color figures

1. INTRODUCTION

Over the past 4 years, some 3600 planet candidates have been found with the *Kepler* mission (e.g., Borucki et al. 2011; Batalha et al. 2013; Burke et al. 2014). Approximately 1350 of these reside in multiplanet systems. The observed orbital period distribution peaks at ∼4 days and 80% of the planets are found in the orbital period range $P_{\rm orb} = 2.5$–70 days. The falloff toward longer periods is due to observational selection effects, i.e., the probability of a transit decreases roughly as $P_{\rm orb}^{-2/3}$, and the duty cycle of the transits has the same dependence on $P_{\rm orb}$. Toward the short-period end, planets of an Earth radius or larger have a *higher* detection probability because of the increasing number of transits observed, and yet their numbers are falling due to nonobservational selection effects.

Through the work of a number of teams, there have now been more than 100 planets and planet candidates discovered to date with periods between 4.2 hr and 1 day (Léger et al. 2009; Winn et al. 2011; Batalha et al. 2011; Muirhead et al. 2012; Rappaport et al. 2012; Ofir & Dreizler 2013; Huang et al. 2013; Sanchis-Ojeda et al. 2013, 2014; Rappaport et al. 2013; Jackson et al. 2013). Thus far, all planets found with $P_{\rm orb} \lesssim 3/4$ day are small, i.e., $\lesssim 2\,R_\oplus$, and potentially rocky. There are a number of reasons why larger planets cannot easily survive in such short-period orbits. Among the pitfalls of being a short-period gas giant are tidally induced orbital decay (Rasio & Ford 1996; Schlaufman et al. 2010), a possible tidal-inflation instability (Gu et al. 2003a), Roche-lobe overflow (Gu et al. 2003b; Ford & Rasio 2006), and evaporation (e.g., Murray-Clay et al. 2009; Sanz-Forcada et al. 2011). An Earth-mass rocky planet would be less susceptible to these effects, and in particular, the rocky portion of the planet might survive evaporation nearly indefinitely (Perez-Becker & Chiang 2013). In this regard, several hot-Jupiters have been observed to be losing mass via gaseous emissions, e.g., HD 209458b (Vidal-Madjar et al. 2003; Yelle 2004; García-Muñoz 2007; Murray-Clay et al. 2009; Linsky et al. 2010) and HD 189733b (Lecavelier des Etangs et al. 2010).

Thus far, only one exoplanet has shown evidence for mass loss via dusty effluents—KIC 1255b (Rappaport et al. 2012). The size of the underlying planet is inferred to be quite small (perhaps nearly lunar size) because of the theoretical difficulty of removing dust grains from planets with a substantial gravity (Perez-Becker & Chiang 2013).

In this work, we report on a second planet candidate that appears to also be emitting dusty material—KOI-2700b. This object is in a 21.84 hr orbit about a mid-K host star (KIC 8639908). The presence of a dust tail is inferred via a distinctly asymmetric transit profile. In Section 2, we present the observational evidence for a dust tail in KOI-2700 using 16 quarters of long-cadence, and 2 quarters of short-cadence, *Kepler* data. The asymmetry in the transit is apparent by eye but we fit the transit profile to a mathematical (i.e., nonphysical) model and quantify the degree of asymmetry. In this same section, we also describe a number of tests and sanity checks that we have performed on the data. In Section 3, we present a new method for extracting the flux time series from point-spread-function (PSF) fitting of the images at the pixel level. These results are used to confirm our findings with the more conventional *Kepler* data products. A semiphysical dust-tail model is developed and utilized in Section 4 to fit the transit. This section includes a description of the dust-tail trajectories, a discussion of the scattering and absorption cross sections for the likely dust material, and a

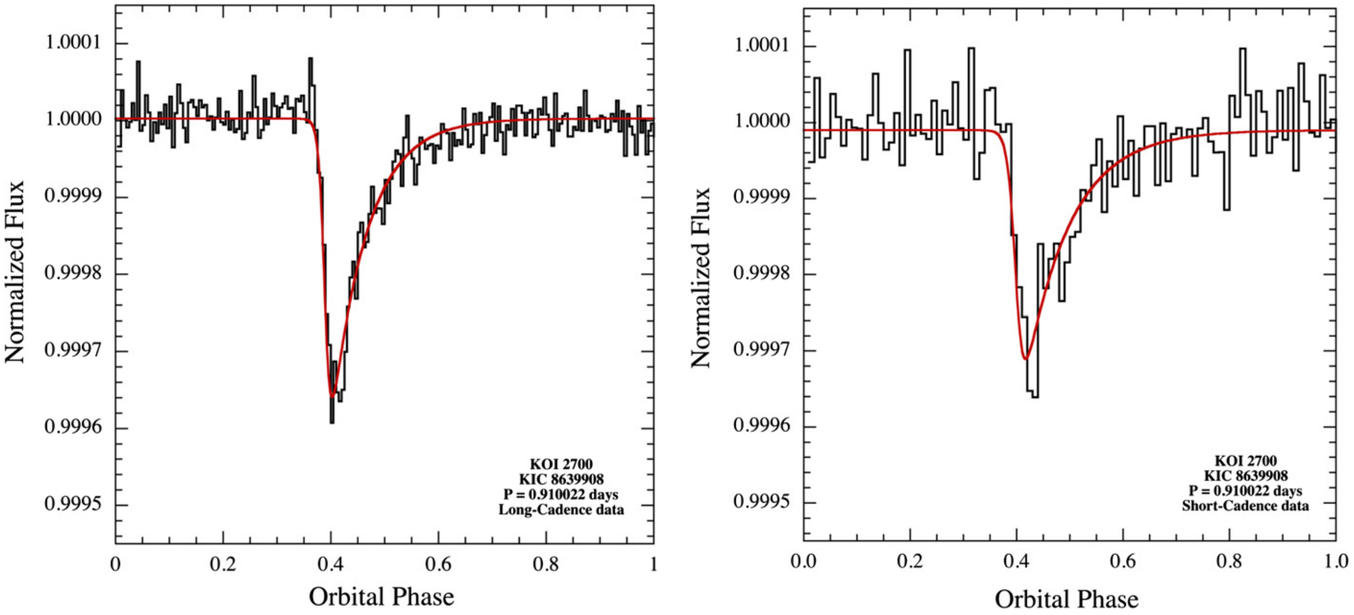

Figure 1. Left: folded light curve of KOI-2700b for 16 quarters of long-cadence data in 200 bins (6.5 minute each). The red curve is a fit to a nonphysical model (see the text). Right: same as left panel but using 2 quarters of short-cadence data in 100 bins (13 minute each). The red curve is a fit to the same nonphysical model as in the left panel.

(A color version of this figure is available in the online journal.)

calculation of the values of β, the ratio of radiation-pressure forces to gravity, that are likely to obtain in the vicinity of KOI-2700. The fitted transit parameters are discussed at the end of that section, with emphasis on a few of the parameters that have significant physical interpretation. Finally, we summarize our results and draw a number of conclusions about this system in Section 5.

2. TRANSITS OF KOI-2700

2.1. Data Retrieval and Preparation

We utilized Q1 through Q16 of the *Kepler* long-cadence (LC) data as well as the two existing quarters (Q14 and Q15) of short-cadence (SC) data for KOI-2700. The long-cadence and short-cadence durations are 29.4 and 0.98 minutes, respectively. Most of the light curves used for this study have been produced with the simple aperture photometry (SAP_FLUX) data. The time series from each quarter was divided by its median value. Then, the normalized data from all quarters were stitched together into a single time series.

Stellar variability and instrumental signals were filtered out as follows. For each data point in the flux time series, $f(t_j)$, a linear function of time was fit to all the out-of-transit data points at times t satisfying $|t - t_j| < P_{\rm orb}/2$, where $P_{\rm orb}$ is the orbital period. Then, $f(t_j)$ was replaced by $f(t_j) - f_{\rm fit}(t_j) + 1$, where $f_{\rm fit}$ is the best-fitting function. This approach is quite efficient at filtering out any variability on timescales longer than the orbital period, while hardly affecting the transit profile.

To determine the orbital period, we first utilized a Lomb–Scargle transform with the frequencies oversampled by a factor of 20. We then fit a linear function to the peak of the base frequency and the peaks of the next twelve higher harmonics. The best determined period is $P_{\rm orb} = 0.910023 \pm (4 \times 10^{-6})$ days. From this same transform, but before filtering, we determined that the rotation period of KOI-2700 is $P_{\rm rot} = 10.98 \pm 0.02$ days. We also used a box least squares transform (“BLS”; Kovács et al. 2002) to search for other planets in the system but could only set limits on the transit depths of $\sim 100\,(P_{\rm orb}/{\rm days})^{1/3}$ ppm.

We also determined the orbital period via a different approach. Here, we carried out an oversampled grid search of periods via epoch folding and measuring χ^2 for the hypothesis that there are no systematic deviations from a constant flux in the folded light curve. Values of χ^2 are mapped out versus trial period, and the maximum χ^2 determines the most likely period; the shape of the χ^2 profile and the number of bins in the fold determine the uncertainty in the period. The best-fit period via the trial folds is $0.910022 \pm (5 \times 10^{-6})$ days.

2.2. Average Light Curves

The 16 quarters of long-cadence filtered data for KOI-2700 were epoch-folded about the best determined period of $P_{\rm orb} = 0.910022$ days. The folded data were then averaged into 200 bins per orbit, corresponding to a bin width of 6.5 minutes. The results are shown in Figure 1 (left panel). The transit profile is obviously quite asymmetric, with a sharp ingress and much longer egress tail. The corresponding light curve produced from the two available quarters of short-cadence data are shown in the right panel of Figure 1. Because of the lower statistical precision of the short-cadence data (by a factor of $\sim\sqrt{8}$ due to the $\times 8$ shorter baseline), we put the folded data into only 100 phase bins. In spite of the reduced statistical precision of the short-cadence data, the same asymmetry of the transit profile is quite clear in the SC data.

For purposes of quantifying the depth and asymmetry of the transit profile, we fit a nonphysical mathematical function to the transit profiles. The function we adopted is an “asymmetric hyperbolic secant” (see, e.g., Ruan et al. 2000):

$$T(\theta) = F_0 - C[e^{-(\theta-\theta_0)/\theta_1} + e^{(\theta-\theta_0)/\theta_2}]^{-1}, \tag{1}$$

which has five free parameters: F_0 is the out-of-transit flux, C is related to the transit depth, θ_0 is a measure of orbital phase zero, and θ_1 and θ_2 are the characteristic angular durations of the

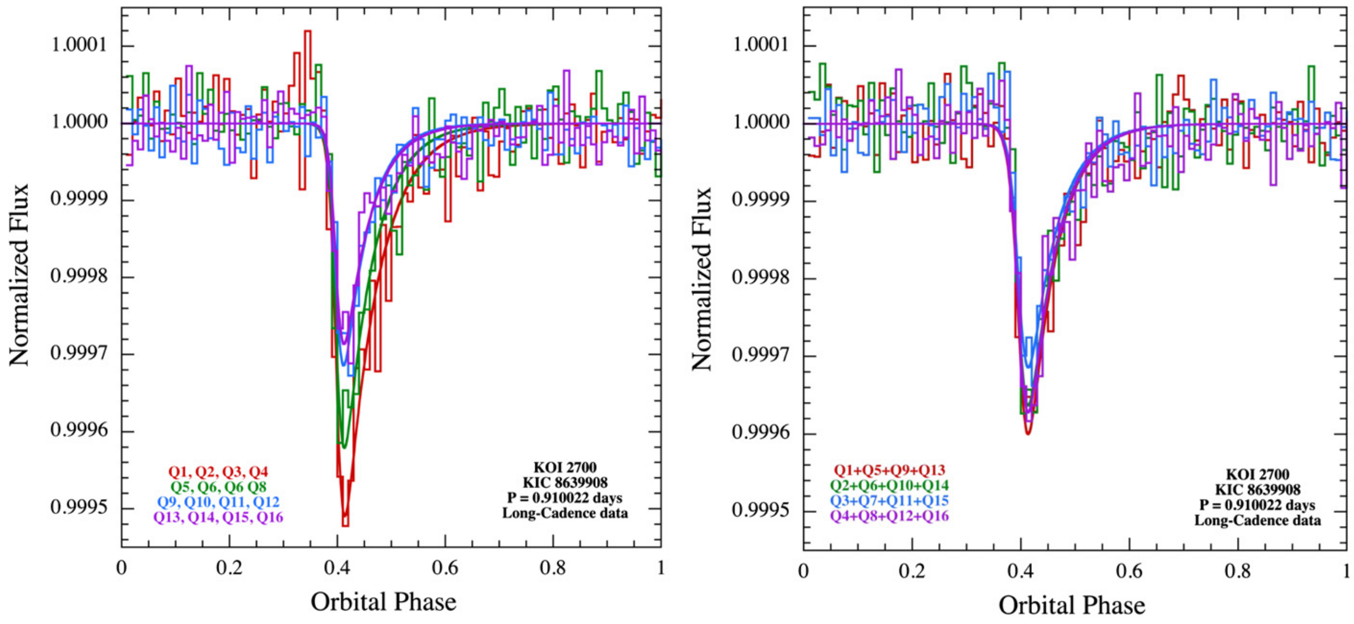

Figure 2. Left: folded light curves for KOI-2700b broken up by years elapsed into the *Kepler* mission. Note the dramatic decrease in transit depth with time. Right: folded light curves of KOI-2700b divided according to *Kepler* season (i.e., the spacecraft rotation angle). Both the transit depth and shape are roughly independent of season.

(A color version of this figure is available in the online journal.)

ingress and egress, respectively. The minimum of this function occurs near θ_0 but with an offset and a depth given by:

$$\text{offset} = \theta_1\theta_2 \ln(\theta_2/\theta_1)/(\theta_1 + \theta_2)$$

$$\text{depth} = \frac{C\mathcal{R}^{\mathcal{R}/(1+\mathcal{R})}}{(1+\mathcal{R})},$$

where $\mathcal{R} \equiv \theta_2/\theta_1$. In the limiting case where $\theta_2 = \theta_1$, this function reduces to a conventional hyperbolic secant with an offset equal to 0 and a depth of $C/2$.

Applying this fit to the long-cadence data yields $\theta_1 = (7.0 \pm 0.7) \times 10^{-3}$ and $\theta_2 = (6.6 \pm 0.35) \times 10^{-2}$, where the θ's are expressed in units of orbital phases. The ratio of θ_2/θ_1, a direct measure of the asymmetry of the transit, is 9 ± 1 but note that this value is really only a lower limit since the transit ingress is not well resolved with the LC data. The fitted value of the constant, C, plus the ratio $\mathcal{R}$, translate to a mean transit depth of 360 ± 15 ppm (over the four years of the *Kepler* mission).

2.3. Variations with Kepler Season and with Time

The relatively small transit depth for KOI-2700b does not readily permit an analysis of the transit-to-transit variability as could be done for KIC 1255b (see, e.g., Rappaport et al. 2012; Kawahara et al. 2013). However, it is straightforward to check if there is a systematic variation of the transit profile or depth with time. To this end, we divided the *Kepler* long-cadence data up into four approximately equal segments of four quarters each. The results are shown in Figure 2 (left panel). As is clearly evident, the transit depth is decreasing systematically with time over the duration of the *Kepler* mission. The transit depths are: 525, 449, 305, and 308 ± 25 ppm, respectively, decreasing with year during the *Kepler* mission. Moreover, θ_2, the "recovery angle" for the tail of the egress, generally becomes systematically smaller with year (see Table 1).

We also constructed epoch-folded light curves of KOI-2700b according to the four *Kepler* "seasons," i.e., by the rotation angle of the spacecraft. These results are shown in Figure 2 (right panel). We see that there are no obvious changes in either the shape or the depth of the transits with *Kepler* season (see Table 1). We actually *do* expect to see a small change of ∼50 ppm from season 0 to season 3, separated on average by 9 months (due to the approximately linear trend in the transit

Table 1
Parameters Fits to AHS[a] Model

Epoch	C[b]	θ_1[c]	θ_2[d]	Depth[e]
LC data	493	0.0070	0.0655	360
SC data	419	0.0070	0.0860	321
year 1[f]	716	0.0070	0.0669	525
year 2[f]	625	0.0070	0.0613	449
year 3[f]	465	0.0070	0.0400	305
year 4[f]	452	0.0070	0.0473	308
season 0[g]	627	0.0070	0.0532	438
season 1[g]	508	0.0070	0.0547	357
season 2[g]	555	0.0070	0.0603	397
season 3[g]	565	0.0070	0.0537	395
PSF fluxes	471	0.0068	0.0598	339

Notes.

[a] Nonphysical mathematical fitting function we have called an "asymmetric hyperbolic secant" (see also Ruan et al. 2000).

[b] See Equation (1) for definition. Units are in ppm. Typical uncertainties are 8%.

[c] Fixed at the value found from the fit to all 16 quarters of the LC data. The egress is too steep to be resolved in the LC data, and there is insufficient statistical precision in the SC data to improve upon the determination of θ_1. For the PSF data set, θ_1 was allowed to be a free parameter. Units are in orbital cycles.

[d] Angle characterizing the egress tail; typical uncertainty of ∼6%–10%. Units are in orbital cycles.

[e] Transit depth expressed in ppm; typical uncertainty of ∼8%.

[f] Year of the *Kepler* mission.

[g] *Kepler* spacecraft rotational season.

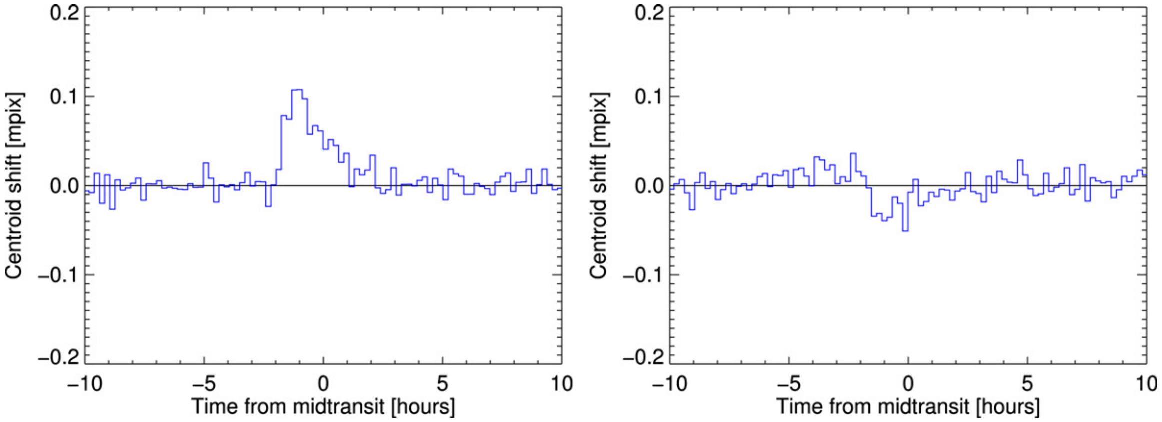

Figure 3. Left: image centroid shift of the column position for KOI-2700b folded with the period of 0.910022 days. The ∼110 micropixel shift is due to the presence of a neighboring star that is 6.″6 away from the target star but ∼2 mag brighter. Right: image centroid shift of the row position for KOI-2700b exhibiting a corresponding −40 micropixel shift.

(A color version of this figure is available in the online journal.)

depths with time). However, this change is approximately within the statistical uncertainty of the measurements.

The transit parameters found from the asymmetric hyperbolic secant fit are summarized in Table 1 for all 4 years and all 4 *Kepler* seasons as well as the summed 16 quarters of LC and 2 quarters of SC data.

In spite of the shallow transit depths in KOI-2700, we did search, on a statistical basis, for depth fluctuations during various portions of the transit in comparison to the rms fluctuations in flux outside of transit. We use the unbinned folded light curves to measure the rms fluctuations in the out-of-transit flux during an orbital phase interval of 0.15. These were compared with the rms fluctuations during portions of the transit that were of various durations between 0.05 and only 0.015 in orbital phase. We then computed the ratio of the in-transit to out-of-transit rms fluctuations. If there were no transit-to-transit depth variations, we would expect a ratio of unity, at least to within the statistical uncertainties. We computed this ratio for each of the four *Kepler* mission years separately and found the following ratios of rms fluctuations in-transit to out-of-transit: 1.27, 1.21, 1.18, and 1.25 (all ±0.03). On the face of it, this does seem to provide evidence for transit depth fluctuations slightly above those which would be due to the secular decrease observed during the *Kepler* mission (i.e., about 15% per year). However, we note the following caveat. There is a tradeoff between utilizing a large part of the transit (to gain statistical precision) at the expense of increasing the rms because of the changing depth during the transit egress and taking only a narrow slice of the transit which reduces the statistical precision. In any case, we take approximately 20% as a nominal value for, or upper limit on, the transit-to-transit depth variations.

2.4. *Possible Sources of Light Contamination*

As is customary, we checked the image light centroid of the target star, KIC 8639908, in phase with the transits in order to ascertain whether the source of the dips is indeed the target star (Jenkins et al. 2010). We filtered the time series of the photocenter row and column pixel coordinates in the same manner that was described in Section 2.1 for the flux time series. We then calculated the mean of the in-transit coordinate, the mean of the out-of-transit coordinate, and the differences between those means, which we denote dx and dy. Figure 3 (left panel) shows the centroid data for the column position folded with the 0.910022 day period. It is clear that the light centroid shifts in the positive column direction by an amount $dx \simeq 110$ micro-pixels during the times of the transits compared to the out-of-transit times (Figure 3, left panel). There is also a smaller shift of the light centroid in the row direction of $dy \simeq -40$ micro-pixels (Figure 3, right panel). The mean transit depth is $df \simeq 360$ ppm. We then examined the ratios dx/df and dy/df. When these are multiplied by the pixel size (4″), one obtains the angular offset between the source of the transits and the out-of-transit image photocenter (see, e.g., Jenkins et al. 2010). The magnitude of the angular offset is ∼1.″3. One can then compare this offset during transits to the locations of the stars revealed in the electronically available UKIRT images[6] of the *Kepler* field.

An inspection of the UKIRT *J*-band image of this region (see Figure 4, right panel) indicates that, in addition to the $J =$ 13.58 mag star at the location of the target star, KIC 8639908, there is a neighbor star (KIC 8639919) about 1 mag brighter in *J*-band at a distance of 6.″6 to the southeast. For the two stars in question, each has its *own* pixel mask and photometric aperture. During each quarter, the photometric aperture for KIC 8639908 is chosen to optimize the signal of the target while minimizing the flux leakage from the brighter neighbor star (i.e., maximizing the signal-to-noise ratio) in the production of the SAP_FLUX time series.

As an illustration of the pixel mask geometry, we show the pixel mask for the neighbor star KIC 8639919 in Figure 4 (left panel), which also contains KIC 8639908 (KOI-2700). The geometry of that mask, in relation to the target and the neighbor star, is shown with the location of the various KIC sources indicated.

The net centroid shift of ∼120 micro-pixels during the time of transits (using the KIC 8639908 aperture data) corresponds to a difference of ∼1.″3 between the light centroid and the source of the transits. The direction of that vector points from the target star to the bright neighbor, thereby indicating that the target star, KOI-2700, is the likely source of the transits.

We added a complementary verification that KOI-2700 is the source of the transits by analyzing the flux time series from the photometric aperture of the bright neighbor (KIC 8639919) which shows *no evidence* for transits.

---

[6] http://keplerscience.arc.nasa.gov/ToolsUKIRT.shtml

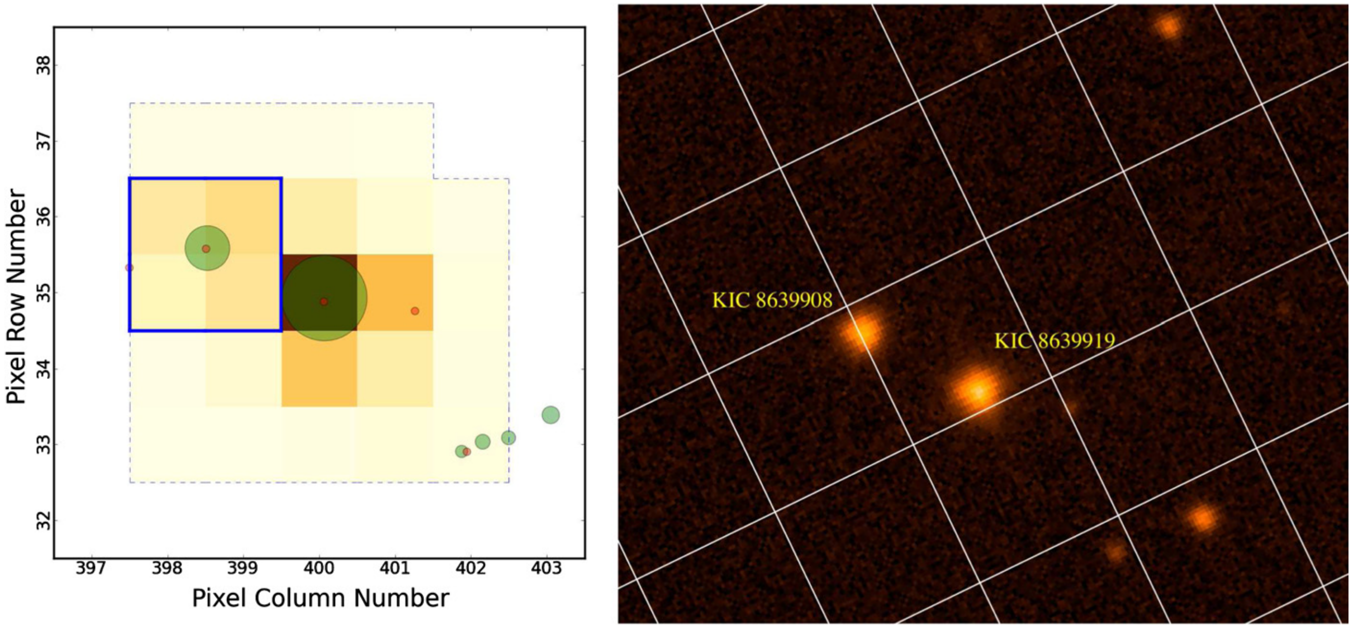

Figure 4. Left: an illustrative observational schematic at the pixel level from Q4. The dashed line contains the pixel mask for KIC 8639919, while the solid line is an 8″ × 8″ photometric aperture centered on KIC 8639908. This pixel mask is actually for the brighter neighboring object at {400, 35} that is ∼6″.6 to the southeast of KIC 8639908 at {398.5, 35.7}; both objects happen to be contained in the same pixel mask. Green circles are KIC sources, and red circles are source detections from other catalogs. The objective is to disentangle the fluxes from the target star and its neighbor which is ∼2 mag brighter. Right: UKIRT *J*-band image of the KOI-2700 region showing the target star and its brighter neighbor. The orientation here is the same as for the schematic on the left. The grid lines are 8″ × 8″ and represent R.A. and Decl., with north pointing toward the lower left and east to the lower right.

(A color version of this figure is available in the online journal.)

3. PSF-PHOTOMETRY OF THE DATA AT THE PIXEL LEVEL

As an important check on the photometry of the target star and its brighter neighbor, we also made use of the data at the pixel level.

There is some potential for the variable depth of the transits observed over time to be a systematic artifact of the archived SAP_FLUX and for systematic errors to occur in the absolute depth of the transits. Artifacts would be a product of the source confusion within the photometric pixel aperture, especially if the wings of a bright contaminating neighbor star are comparable to, or even outshine, the target star. In SAP_FLUX data, there is no attempt to correct for systematic flux deviations due to source crowding. To test the fidelity of the transit behavior inferred from the SAP_FLUX data, we employed a new technique to derive a complementary sequence of light curves by fitting a point-spread-function (i.e., "PSF") model to the calibrated pixel-level flux from each of 62,000 individual exposures across quarters Q1–Q16. The empirically determined combined differential photometric precision (CDPP; Christiansen et al. 2012) of the PSF photometry for KOI-2700, with a median value of 147 ppm (with a 6 hr window), is slightly inferior to the precision of the SAP_FLUX data (median CDPP = 124 ppm)—a consequence of the limitation in the precision of the PSF model. However, we show that PSF photometry successfully deconvolves the two confused sources (KOI-2700 and its bright neighbor), confirms the observation of monotonically decreasing transit depths, and yields approximately the same average transit depth that is obtained from the SAP_FLUX data from the pixel mask and photometric aperture for KIC 8639908.

3.1. *The Basic PSF-Fitting Technique*

With a number of caveats noted below, we assume that the pixels within the target mask of KOI-2700 can be characterized as two PSFs of independent magnitude and position (see Figure 5). We then minimize upon the uncertainty-weighted residuals between the data and the fit in order to yield the flux and pixel position of both sources for every exposure across Q1–16. More specifically, there are two unknown shifts of the photometric aperture relative to the sky ($\Delta\alpha$ and $\Delta\delta$) and two unknown source fluxes that can be determined via a χ^2 fit to the intensities in four or more pixels (see Figure 5).

The *Kepler* PSF was calibrated from dithering observations during the commissioning phase of the mission (Bryson et al. 2013). The PSF is stored as a set of pixel-value lookup tables at the MAST archive.[7] Due to optical aberrations, the PSF varies in shape across the field-of-view. Each CCD channel has five PSF models associated with it: one for the center of the channel and one for each corner. While the models are of high statistical precision, their employment introduces two main sources of systematic error. First, the shape of the PSF must be interpolated to the target position from this relatively coarse grid of models. Second, telescope focus is temperature-dependent. The thermal state of the spacecraft changes as the sun-angle of the telescope boresight varies across the orbit and after spacecraft maneuvers. Therefore, the accuracy of the commissioning calibration is a function of the thermal state of the spacecraft.

For much more detail on how the PSF-fitting algorithm works and is implemented, see M. Still & T. Barclay (2013, in preparation).

3.2. *PSF-photometry Results*

We utilized the PSF-photometry to confirm the mean transit depth of KOI-2700 as well as the secular decrease in transit depth with time. In Figure 6, we show an epoch-folded light curve of the PSF-photometry for the target star, KOI-2700. The familiar

---

[7] http://archive.stsci.edu/kepler/fpc.html

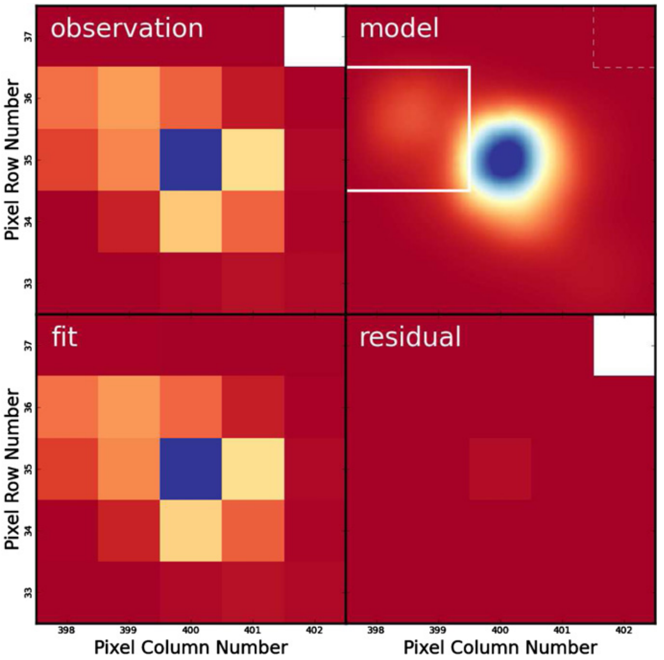

Figure 5. Top left is a typical 29.4 minute LC observation of the target, for one particular frame of 62,000 exposures. The blue pixel at {400, 35} contains KIC 8639919 that is ∼2 mag brighter than the target KOI-2700 located at {398.5, 35.7}. During this quarter, the target fell upon detector module 17 output node 3. The best PSF model fit is plotted in the top right, while that fit, rebinned across the detector pixels, is compared at the lower left. The lower right panel contains the residuals between the data and the best fit. All images are plotted on a linear intensity scale. PSF-derived light curves are constructed by repeating this fit for every exposure over quarters 1–16.

(A color version of this figure is available in the online journal.)

asymmetric transit profile seen in the SAP_FLUX photometry is nicely reproduced. Superposed on this plot is the epoch-folded light curve using PSF-photometry for the bright neighbor star. There is no trace of any transit. This is yet another demonstration that we have identified the correct star that is being transited. More importantly, the PSF-photometry confirms, though with somewhat weaker statistical precision, that the transit depths are indeed *decreasing* with time during the *Kepler* mission. These relative decreases in flux are in close agreement with those listed in Table 1 for the SAP_FLUX data.

Finally, we note that the transit profile shown in Figure 6 for KOI-2700, produced with the PSF-fitted flux series, has a transit depth of 340 ppm. This is within the statistical uncertain of the mean transit depth obtained from the SAP_FLUX data (see Table 1).

Because the PSF-fitting technique is just being developed, we continue to utilize the results obtained with the SAP_FLUX data for the remainder of this study, though the results from the two data sets are in excellent overall agreement.

4. MODEL FITS

We now proceed to analyze the asymmetric transit profile of KOI-2700b under the assumption that the transit is the result of a very small planet that is trailing a dust cloud which is largely responsible for the optical extinction. This model is motivated by the dust tail that is inferred to be present in KIC 1255b (Rappaport et al. 2012; Brogi et al. 2012; Budaj 2013). In any such comet-tail like model, the effective optical thickness of the dust tail is assumed to decrease monotonically with angular distance from the emitting planet. The falloff in optical thickness is due to four possibilities: (1) a decrease in the density of dust grains due to an apparent increase in angular velocity with distance from the planet (i.e., inferred from the continuity equation); (2) a decrease in the diameter of the particles and hence, a concomitant decrease in cross section, as the particles sublimate; (3) unlikely geometric broadening of the dust tail perpendicular to the orbital plane so that it ultimately covers more than the diameter of the host star; and (4) possible removal by stellar winds. We discuss some effects of stellar winds separately in Appendix A and conclude that this is not likely to have a large effect on the dust tail (see, e.g., Cohen et al. 2011; Bisikalo et al. 2013 for a related discussion of the interaction of stellar winds with *gaseous* emissions from planets).

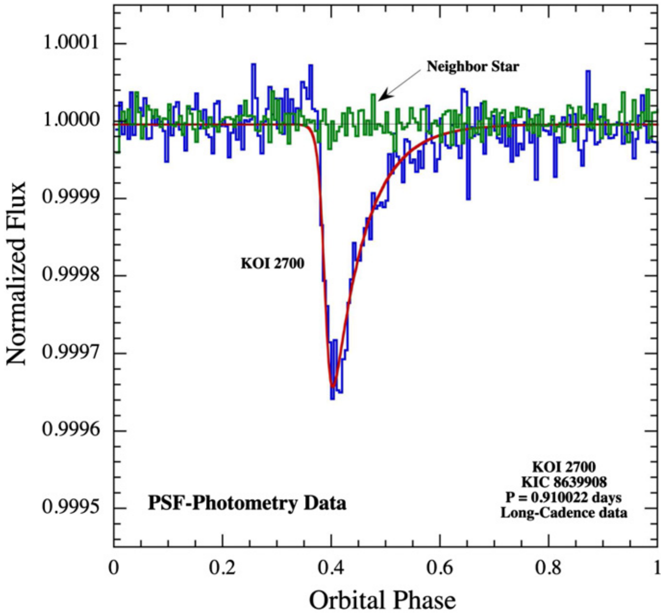

Figure 6. Epoch-folded transit profile produced from PSF photometry at the pixel level for KIC-2700 (blue curve) and for the nearby bright neighbor star (green curve). There is no trace of the transit in the photometry from the neighboring star.

(A color version of this figure is available in the online journal.)

4.1. *Motion of the Dust Particles*

We can gain some considerable insight into the shape of the dust tail and the angular velocity versus angular distance by considering an idealized problem. If the dust particles are ejected from the planet with a velocity that is comparable with the escape speed from the planet, then initially the liberated dust will be moving with basically the same orbital velocity as the planet. The ratio of planet escape speed to orbital speed is $\sim\sqrt{M_p a_p / M_s R_p}$, where M_s and M_p are the masses of the host star and the planet, respectively, R_p is the radius of the planet, and a_p is the orbital radius of the planet. If the mass ratio of star to planet is several hundred thousand, then this factor completely outweighs the small ratio of planet radius to orbital radius. Thus, once the dust is free of the planet's gravity, it is essentially initially at rest with respect to the planet in its motion about the host star.

A liberated dust particle is then subjected to radiation pressure from the host star.[8] For a given dust particle, the ratio of

---

[8] For a brief discussion of the potential effects of a stellar wind on the dust, see Appendix A.

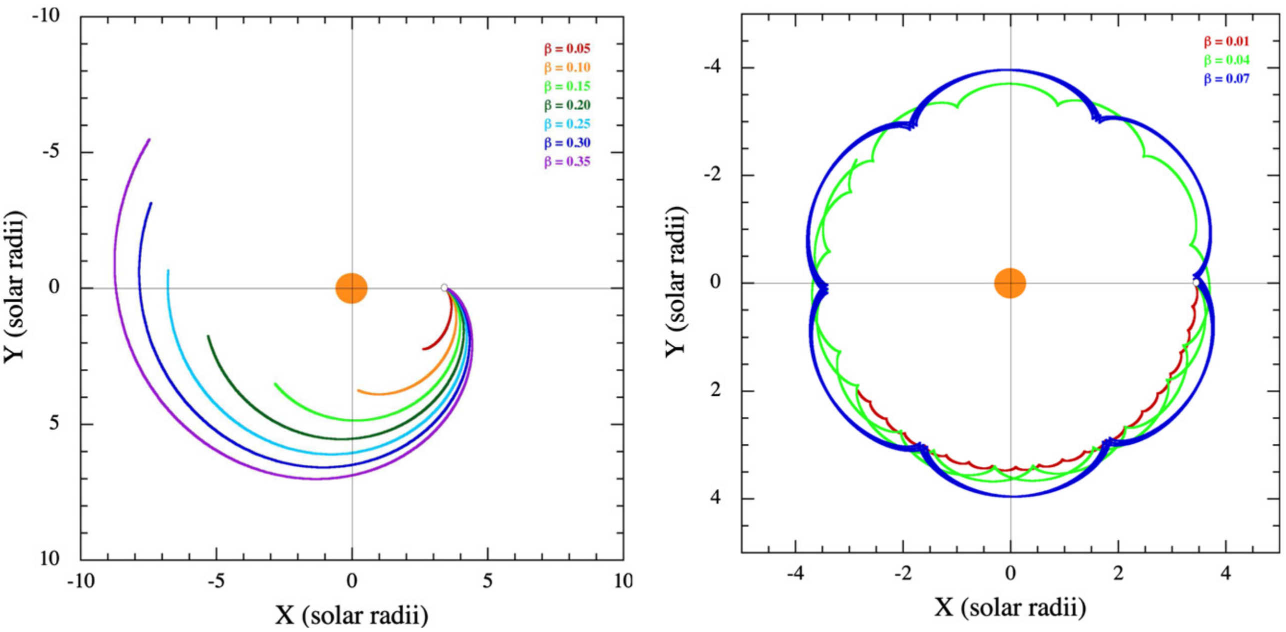

Figure 7. Left: dust particle trajectories in the rest frame of the orbiting planet for different fixed values of β, the ratio of radiation pressure forces to gravity (see the text). The duration of the dust trail is arbitrarily cut off after one orbital cycle of KOI-2700b (i.e., a duration of 0.91 days). The filled orange circle is supposed to represent the host star to approximately the correct scale. Right: same as the left panel but for smaller values of β. These dust particle trajectories are followed for 20 orbital periods of the planet. The cusps represent periastron passages of the dust particles where the instantaneous angular velocity of the dust equals that of the planet and the density would be enhanced.

(A color version of this figure is available in the online journal.)

radiation-pressure force to gravity is designated as β. Thus, ideally, the dust particle finds itself in an effectively reduced gravitational field compared to that of the planet, with $g_{\rm eff} = GM_s(1-\beta)/r^2$. The resultant orbit of the dust particle is a Kepler ellipse with a periastron point at the location where it was released. The eccentricity, e, semimajor axis, a_d, and orbital angular frequency, ω_d, of the dust particle are straightforward to work out:

$$e = \frac{\beta}{1-\beta}; \quad a_d = a_p \frac{1-\beta}{1-2\beta}; \quad \omega_d = \omega_p \frac{(1-2\beta)^{3/2}}{1-\beta} \qquad (2)$$

(see Appendix B for a derivation). Moreover, the angular velocity of the dust particle with respect to the planet is given by a closed-form, analytic expression:

$$\omega_p - \dot{\theta}_d = 2\omega_p \beta \,(2 - \beta + \beta \cos\theta_d) \sin^2(\theta_d/2), \qquad (3)$$

(see Appendix B for a derivation) where ω_p is the orbital frequency of the planet, and θ_d is the angular distance traveled by the dust particle in inertial space after its release. If any quantities are needed as an explicit function of time, then it is straightforward to solve Kepler's equation.

Some illustrative dust particle trajectories in the rest frame of the orbiting planet are shown in Figure 7 (left panel) for several different fixed values of β, the ratio of radiation-pressure force to gravity, over the range of $\beta = 0.05$–0.35 ($\beta > 0.5$ leads to an unbound orbit). The duration of the dust trail is arbitrarily cut off after one orbital cycle of KOI-2700b (i.e., a duration of ~22 hr). Since the transit duration is at least 5–6 hr long, i.e., ~25% of the orbital cycle, this would require a value of $\beta \gtrsim 0.1$ (see Figure 7) unless the dust can last for $\gtrsim$22 hr in the intense radiation field of the host star.

We learned from simulations carried out for the study of KIC 1255b (Rappaport et al. 2012), that the dust particles remain in a rather tight ribbon (with respect to the orbital plane) as they stream away from the planet, nearly regardless of the value of β. Thus, we expect from an argument involving the continuity equation, that the density of dust particles must necessarily thin out in proportion to $1/(\omega_p - \dot{\theta}_d)$ as the particles pick up angular speed with respect to the planet, assuming they are injected into the tail at a constant rate.

Thus, we might hope that the inverse of Equation (3) would provide a good estimate of the density variation of dust particles along the tail (assuming there were no sublimation and no important effects from stellar winds). If we wish to write this expression as a function of $\Delta\theta$, the angular distance between the dust particle and the planet, this requires the solution of Kepler's nonlinear equation at every point. However, an approximate transformation between θ_d and $\Delta\theta$ involves only the simple scaling relation:

$$\begin{aligned} \theta_d &\simeq \Delta\theta \frac{\omega_d}{\omega_{\rm syn}} = \Delta\theta \frac{P_p}{P_d - P_p} \\ &= \Delta\theta \, \frac{(1-2\beta)^{3/2}}{1-\beta-(1-2\beta)^{3/2}} \simeq \frac{\Delta\theta}{2\beta}, \end{aligned} \qquad (4)$$

where $\omega_{\rm syn}$ is the synodic orbital period of the dust with respect to the planet ($\omega_{\rm syn} \equiv \omega_p - \omega_d$), and P_d and P_p are the orbital periods of the dust particle and planet, respectively. We see that, for small values of β (see Section 4.2), the factor multiplying $\Delta\theta$ can be quite large.

It is apparent from the transit profiles that the angular extent of the dust tail exceeds 1–2 rad. Therefore, if $\Delta\theta$ in the dust tail where optical extinction is significant ranges from, say, 0–1.5 rad, then θ_d in Equation (3) could well range from 0 to 15 rad for an illustrative value of $\beta = 0.05$ (see Section 4.2). It would then follow that Equation (3) would cycle through several minima, with a concomitant set of maxima in the dust density. However, when one takes into account a range of particle sizes in the dust emitted by the planet, this implies a corresponding range

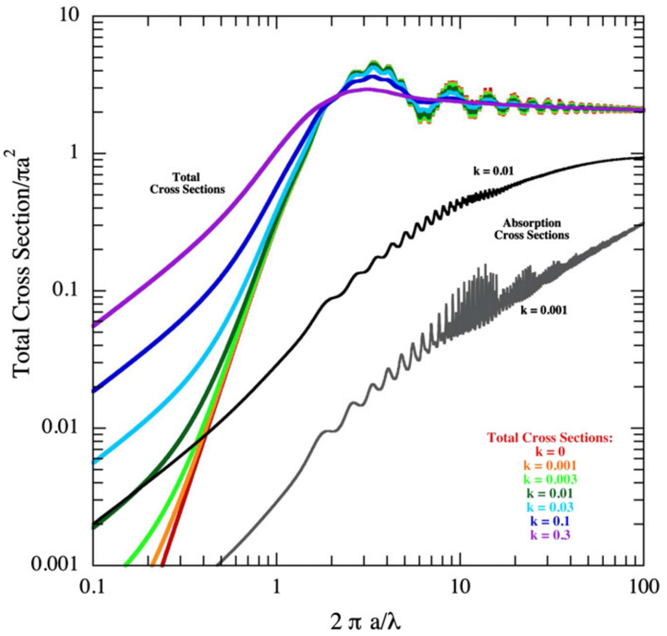

Figure 8. Mie scattering cross sections, normalized to the geometrical area of the particle, as a function of the particle size parameter, $2\pi a/\lambda$, where a is the particle radius and λ is the wavelength of the radiation. The real part of the index of refraction is taken to be $n_r = 1.65$, i.e., representative of materials from which the dust might be made, e.g., pyroxene. For purposes of illustration, the imaginary part of the index of refraction, k, is taken to be a small constant, independent of λ. Total cross sections are shown for six different values of k, while the absorption cross section is illustrated for two different values of k ($k = 0.001$, grey curve; $k = 0.01$, black curve). $k = 0.01$ is a reasonable upper limit to what might be expected for the imaginary part of the index at any relevant wavelength.

(A color version of this figure is available in the online journal.)

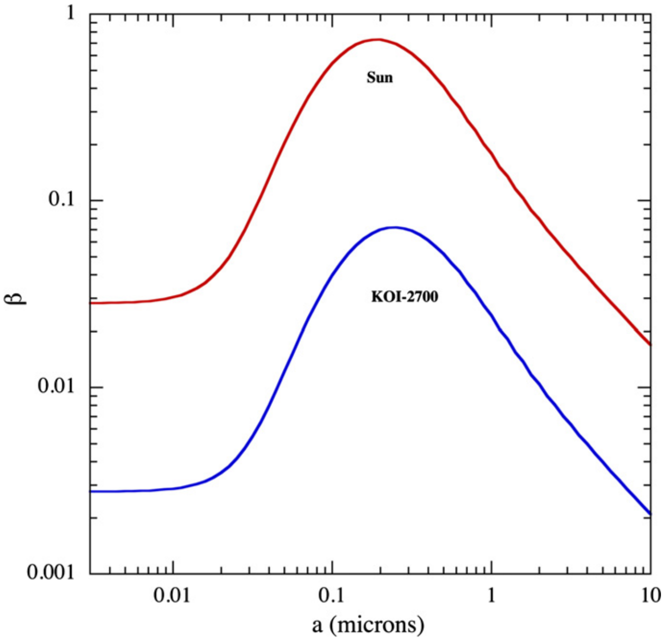

Figure 9. Calculated values of β, the ratio of radiation pressure forces to gravity, as a function of particle size for an assumed composition of pyroxene (blue curve). The indices of refraction used in the calculation are $n_r = 1.65$ and $k = 0.01$, i.e., the same values as were used to produce the green curve in Figure 8. The luminosity and mass adopted to compute $\beta(a)$ in the vicinity of KOI-2700 are $L = 0.09\,L_\odot$ and $M = 0.63\,M_\odot$. The red curve is the same function $\beta(a)$ in the vicinity of the Sun, shown for comparison.

(A color version of this figure is available in the online journal.)

in values of β (which depends sensitively on particle size; see Section 4.2).

As an example of what would ensue with a range of dust particle sizes, we show in Figure 7 (right panel) a set of dust particle trajectories in the rest frame of the planet, for three illustrative particle sizes: $a = 0.2$, 0.1, and 0.05 μm, with corresponding values of $\beta \simeq 0.07$, 0.04, and 0.01 (see Section 4.2).

From the above discussion about the motion of particles of different sizes, we conclude that the periodic enhancements in density along the tail for a given size particle, will tend to be completely washed out by a distribution of particle sizes with their concomitant range of values of β. Therefore, we will simply assume that the density of dust particles is approximately *constant* over the portion of the dust tail that is relevant to the observed asymmetric transit profile. However, this does *not* mean that the attenuation of the dust is constant along the tail. The particles will be subject to sublimation, and their effective cross section drops as their radii become smaller (see Section 4.3); we return to discuss this in Section 4.4 and Appendix C.

4.2. Estimation of β

We approximate the dust particles as spherical and to have a generic real part of their indices of refraction, n_r, equal to 1.65. We take the dust composition to be Earth-abundant refractory minerals such as pyroxenes and olivines. The imaginary parts of the indices of refraction, k, for these materials typically tend to be small (compared to n_r) with relatively modest enhancements at specific wavelengths, λ, but with $k \lesssim 0.01$ at all λ in the range of interest (Kimura et al. 2002, and references therein; Budaj 2013). We utilize a Mie scattering code (Bohren & Huffman 1983) to compute the various cross sections, σ_s and σ_a (scattering and absorption), and $\sigma_{\rm ext} \equiv \sigma_{\rm tot}$, the extinction or "total" cross section for the dust particles as a function of their scaled size (i.e., $2\pi a/\lambda$), where a is the radius of the (assumed) spherical dust particles. The results for $\sigma_{\rm tot}$ are shown in Figure 8 for six different values of the imaginary part of the index of refraction, k (assumed independent of λ, so as to render $\sigma/\pi a^2$ a function of the particle scale size only). As the figure illustrates, the cross section is essentially twice the geometrical area for scale sizes $\gtrsim 2$ but falls roughly as a steep power law for small particle scale sizes. The logarithmic slope, just below particle scale sizes of $\sim$ unity, depends sensitively on the value of k. Two illustrative curves of σ_a versus scaled particle size (for $k = 0.001$ and 0.01) are also shown in Figure 8 for comparison.

We used the cross sections, shown in Figure 8, to compute the value of β as a function of particle size. This requires averaging the cross sections over the radiation spectrum of the host star. Given the level of approximations that have already been made (especially in view of the uncertainties in the chemical composition and shapes of the dust particles), we elected to utilize a simple blackbody spectrum with $T_{\rm eff} = 4433$ K (see Table 2). The results for $\beta(a)$ are shown in Figure 9, with a comparison to $\beta(a)$ in the solar vicinity. The peak value of β occurs for particles of size $\sim$0.24 μm, with a maximum value of $\beta = 0.07 \pm 0.02$ for KOI-2700 (where the error bar arises from the uncertainty in the stellar luminosity and mass). This is in agreement with the results of Kimura et al. (2002), after simply scaling their results for dust particles in the vicinity of the Sun (see their Figure 2). The scaling factor is just

Table 2
Parameters of KOI-2700b and the Host Star

Parameter	Value	Uncertainty
Effective temperature, $T_{\rm eff}$ (K)[a]	4433	±66
Mass of the star, M_s ($M_\odot$)[a]	0.632	±10%
Radius of the star, R_s ($R_\odot$)[a]	0.574	±10%
Surface gravity, log g (cgs)[a]	4.721	0.1
Metallicity, [Fe/H][a]	−0.2	···
Stellar rotation period (days)[b]	10.98	±0.02
Right ascension (J2000)[c]	$19^{\rm h}00^{\rm m}03\overset{\rm s}{.}14$	···
Declination (J2000)[c]	$40°13'14\overset{''}{.}7$	···
K_p mag[c]	15.38	···
g mag[c]	16.44	···
r mag[c]	15.30	···
i mag[c]	14.93	···
z mag[c]	14.69	···
J mag[c]	13.58	···
H mag[c]	12.99	···
K_s mag[c]	12.84	···
Reference epoch for folds (BJD)	2454900.00	···
Orbital period (days)	0.910022	±0.000005
Transit depth (ppm)	305–525[d]	···
Time of transit (BJD)	2454900.358	0.004
Scaled semimajor axis, a/R_s	5.9	±0.4
Impact parameter, b	<1.0	···
Transit "duration" (hr)	>5	2σ
Amplitude of Ellipsoidal light variations (ppm)	<10	2σ
Planet radius, R_p ($R_\oplus$)	<1.06	2σ
Planet mass, M_p ($M_{\rm Jup}$)[e]	<0.86	2σ
Sublimation constant, S[f] (rad^{-1})	2.4 ± 1.0	2σ
β[g], $F_{\rm rad}/F_{\rm grav}$	<0.07	···

Notes.
[a] From Pinsonneault et al. (2012). We assume a plausible uncertainty of 10%.
[b] Derived from the FT of the *Kepler* long-cadence data.
[c] Taken from the Kepler Input Catalog; Batalha et al. (2010).
[d] Variable with time.
[e] Based on absence of ellipsoidal light variations, assuming zero dilution.
[f] From the model fit; see Section 4.
[g] Based on model calculations applicable to KOI-2700.

$(L_s/L_\odot)(M_\odot/M_s) \simeq 0.14 \pm 0.04$. The Kimura et al. (2002) maximum values of β for pyroxene in the solar neighborhood are in the range 0.7–0.8. Using the scaling factor above would yield $\beta_{\rm max} \simeq 0.06$–0.14 near KOI-2700, in fair agreement with our estimates.

4.3. *Sublimation of the Dust*

A substantial difficulty with computing the transmission of the dust tail is that the dust particles will decrease in size monotonically with time due to sublimation in the intense radiation field. As discussed in detail by Kimura et al. (2002), the rate of sublimation depends on the instantaneous grain temperature, which in turn results from a thermal balance between heating and cooling. As the dust particle grows smaller with its sublimation, the absorption cross section decreases, and the value of β changes, as does its orbit.

To obtain a simpler estimate of the sublimation lifetime for the dust particles in KOI-2700, we utilize the results of Kimura et al. (2002) for the lifetimes of cometary dust particles of different sizes and compositions as a function of heliocentric distance. We scale the results in their Figure 4 to the case of the KOI-2700 system. The equivalent heliocentric distance at which to evaluate the grain lifetime is given by: $d_{\rm comet}/R_\odot = (L_\odot/L_s)^{1/2}(a_p/R_\odot) \simeq 11 \pm 2$. At such distances from the Sun, amorphous olivine lasts for only a matter of minutes before it sublimates away; its crystalline counterpart could last hours or more at the nominal equivalent heliocentric distance of 11 $R_\odot$. However, pyroxene grains (amorphous or crystalline) might well last for days even at the lower limit on equivalent distance of 9 $R_\odot$ before sublimating.

See Appendix C for a further discussion of grain sublimation.

4.4. *Transit Model*

For the transit model, we require a function that gives (1) the number density of the dust particles as they thin out due to their changing velocity with respect to the planet and (2) the decreasing scattering cross section due to their sublimation. For the first part, we concluded in Section 4.1 that, for small values of β (appropriate to KOI-2700), use of an approximately constant number density of dust grains over a broad angular range in the dust tail is quite reasonable. Calculation of the reduction in cross section due to sublimation is rather involved and beyond the scope of this paper. In fact, at present there may be insufficient information to compute it in a completely satisfactory way.

Complications in the sublimation-induced changes in the dust-scattering cross sections include the fact that there is an unknown dust particle size distribution (PSD) emitted from the planet and of unknown composition. Furthermore, the particles begin to sublimate with elapsed time after their escape, and their radii change in a complex way. The change in radius depends on the heating and cooling equation (see Appendix C), the imaginary part of the index of refraction, the orbit which, in turn, depends on β, and so forth. The rates of change in particle size cause the PSD to vary with time, which in turn results in the optical thickness of the dust tail decreasing in a highly uncertain way.

In spite of these complications, we have carried out some simplified calculations of the rate at which particles decrease in size due to sublimation; see Appendix C. In the process, we have shown why a simple exponential decrease with time in the effective scattering cross section of the dust grains might be approximately correct.

Thus, to represent the diminution of the grain sizes, and hence scattering cross section, with time and angular distance from the planet, we adopt a somewhat *ad hoc* exponential function with the e-folding angle as a free parameter (see also Rappaport et al. 2012; Brogi et al. 2012; Budaj 2013; Appendix C of this paper). The specific functional form that we adopt to represent the attenuation of the dust tail for any angular distance, $\Delta\theta$, from the planet is:

$$\mathcal{A}(\Delta\theta) = Ce^{-S\Delta\theta} \qquad (5)$$

where $\Delta\theta \equiv \theta - \theta_p$, and θ_p is the angular location of the planet, with $\theta_p = 0$ defined as the point where the planet is midway across the host star. This function has only two free parameters: C, the normalization; and S, the exponential decay factor.

In order to use this transmission function to compute the transit profile, it must be *integrated* across a chord of the host star (for a given impact parameter, b) for each angular location of the planet around its orbit.

The impact parameter, b, is a third free parameter, and the out-of-transit flux, F_0 is a fourth free parameter of the model. We

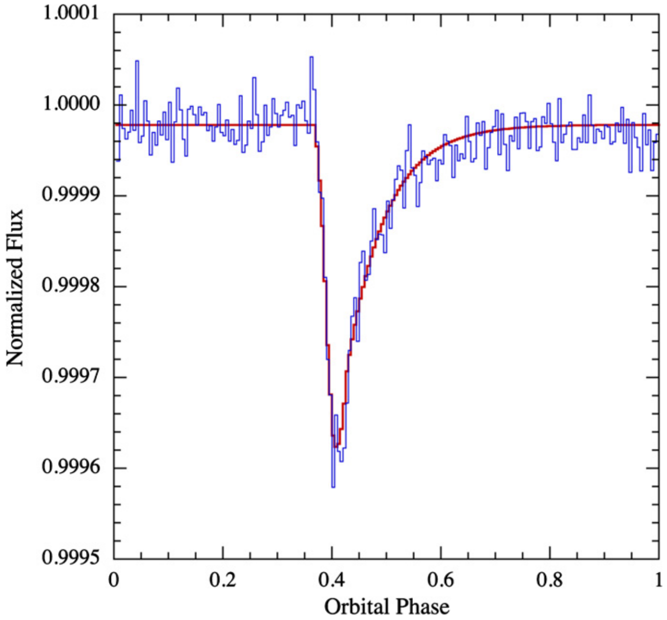

Figure 10. Illustrative model dust-tail fit to the folded long-cadence light curve for KOI-2700b for all 16 quarters (see the text for model parameters). Each of the 200 bins is 6.5 minutes in duration, but the *Kepler* integration time is 29.4 minutes. The model takes the finite LC integration time into account. This particular model fit includes a hard-body planet with radius $R_p = 0.74\ R_\oplus$.

(A color version of this figure is available in the online journal.)

also need to fit for the time (i.e., orbital phase) when $\theta_p = 0$. This is the fifth, and possibly final, parameter in the transit model. As an option, we can also include a hard-body planet attenuator, i.e., the contribution of a conventional transit for a planet of radius R_p.

Finally, we note that because there is no compelling evidence in KOI-2700b for enhanced forward scattering in the transit light curve (as is seen in KIC 1255b; Rappaport et al. 2012; Brogi et al. 2012; Budaj 2013), and due to the generally weaker transit signal in KOI-2700b, we do not include preferential forward scattering into the observer's line of sight in the model.

4.5. *Fitted Parameters*

We used the above model to fit the transit profile for KOI-2700b. The fits are generally quite good, with or without a hard-body planet included, and an illustrative result is shown in Figure 10. Of the six free parameters in the fit, only three of them are of particular physical significance: S, the (assumed) exponential falloff with angle of the effective dust-tail cross section; b, the impact parameter of the dust tail across the host star; and R_p, the hard-body planet radius. The best-fit values are: $S = 2.4 \pm 1.0$ (in units of rad^{-1}), $b < 1.0$, and $R_p < 1.06\ R_\oplus$ (90% confidence limits).

The range of values for b is not constrained at all, as long as the dust tail crosses any part of the host. The angular size of the star, as seen from the vantage point of the planet, is small compared to the angular extent of the dust tail, and therefore, the impact parameter has relatively little effect on the fit. The fitted value of the planet radius yields only an upper limit of $1.06\ R_\oplus$. The reason for the upper limit is the fact that a pure dust tail model fits the transit profile quite well, without the inclusion of a hard-body planet.

We can make use of the fitted transit model parameters to infer something about the lifetime of the dust particles after ejection from the planet. The most probable value of the parameter S is 2.4 rad^{-1}. If we approximate the angle $\Delta\theta$ in Equation (5) by $\Delta\theta \simeq \omega_{\rm syn} t$, where t is the elapsed time for the dust particle to travel from the planet to its current location, then we can define a characteristic decay time for the cross section of the particles by

$$\tau_d \simeq \frac{1}{S\omega_{\rm syn}} \simeq \frac{P_p}{2\pi S}\,\frac{(1-\beta)}{(1-\beta)-(1-2\beta)^{3/2}} \simeq \frac{P_p}{4\pi S\beta}. \quad (6)$$

This implies that the dust in KOI-2700 has a characteristic lifetime against sublimation of $\sim 0.03/\beta$ days, where β can have a range of values between $\sim$0.07 and $\sim$0.01. Thus τ_d likely lies in the range of $\sim$0.5 to 3 days.

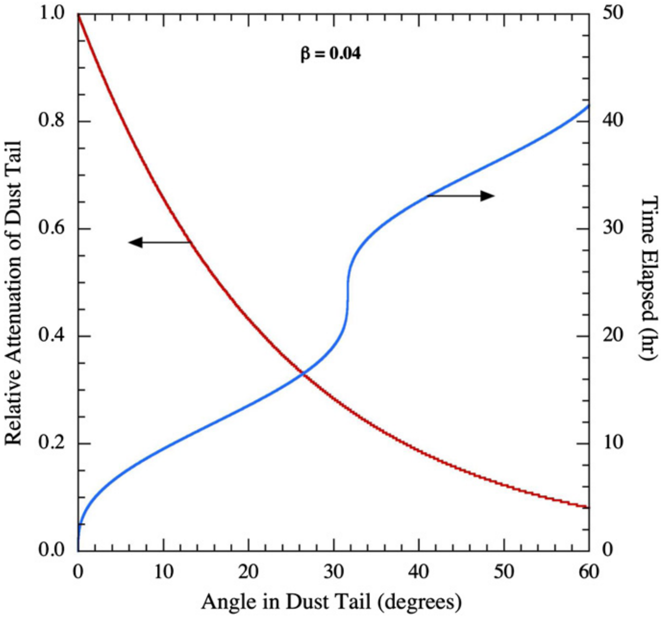

Figure 11. Dust-attenuation portion of the transit model (for an illustrative good fit) is plotted as a function of the angle, $\Delta\theta$, from the planet to the point in the dust tail contributing to the attenuation. The corresponding interval of time required for a dust particle to reach an angular distance, $\Delta\theta$, is also plotted. The time was computed for the illustrative example of $\beta = 0.04$, i.e., the ratio of the radiation pressure to gravity.

(A color version of this figure is available in the online journal.)

In Figure 11, we show an illustrative example of the dust attenuation contribution to the transit function (see Equation (5)) versus the angular distance from the planet to a given point in the dust tail, $\Delta\theta$ (for the case where $S = 2.4$). The attenuation has fallen by a factor of $\sim$10 after 1 rad. On the same plot, we show the time that is required for a dust particle to reach various angles for an illustrative value of $\beta = 0.04$. As can be seen from the figure, it takes $\sim$40 hr for dust to reach an angular distance of 1 rad from the planet. Thus, at least some of the dust in the tail must last for approximately this long before sublimating.

5. DISCUSSION AND CONCLUSIONS

In this work, we have reported on the discovery of a second planet candidate, KOI-2700b, that likely exhibits a dust tail. The optical attenuation of the dust tail appears to decrease monotonically with time during the *Kepler* mission with transit depths ranging between 525 and 305 ppm. This likely implies a decrease in the rate of injection of dusty effluents into the tail by a factor of $\sim$2 over four years. The magnitude of KOI-2700 ($K_p = 15.4$) and the relatively shallow average transit depth (∼360 ppm) make it difficult to study possible orbit-to-orbit fluctuations in the transit depth, as was done in the case of KIC 1255b.

The properties of the host star, KOI-2700 (see Table 2), are quite close to those of the other dust-emitting planet, KIC 1255b. However, there are other planet candidates with $P_{\rm orb} \lesssim 1$ day and with similar host stars (Sanchis-Ojeda et al. 2014) which do *not* exhibit asymmetric transit profiles. The main difference between KOI-2700b and KIC 1255b, in comparison with other short-period rocky planets, may be the *planet mass*. As discussed in Rappaport et al. (2012) and Perez-Becker & Chiang (2013), it is extremely difficult (on theoretical grounds) to remove dust from planets with substantial gravity, e.g., Earth-sized. In particular, Perez-Becker & Chiang (2013) concluded that KIC 1255b is lower in mass than Mercury, and may be as small as the Moon. Our upper limit on the hard body planet in KOI-2700 is $\sim 1.06\, R_\oplus$, consistent with, but not yet limiting this object to lunar size.

The lifetime of such a small planet can be quite short if it loses an Earth mass per Gyr (see, e.g., Rappaport et al. 2012; Perez-Becker & Chiang 2013). However, since KOI-2700b has a transit depth that is, on average, an order of magnitude smaller than that of KIC 1255b, it may be losing mass an order of magnitude more slowly and therefore have a more palatable lifetime (i.e., $\gtrsim 100$ Myr). In Appendix D, we carry out a more detailed estimate of the mass loss rate, $\dot{M}$, of KOI-2700b based on the transit depths and the system parameters as we now understand them. We find a nominal value for $\dot{M}$ of $\approx 6 \times 10^9$ g s^{-1} or ≈2 lunar masses per Gyr.

Because the transit is detectable for nearly a quarter of the 0.91 day orbital cycle, it implies an angular extent of some 90° around the host star. For plausible values of the parameter β, the ratio of radiation-pressure forces and gravity, more than about a day is required for a typical dust particle to move 90° away from the planet. Known abundant minerals that can possibly last this long in the intense radiation field of the host star (at a distance of ∼6 stellar radii) include pyroxine and crystalline olivine (see, e.g., Kimura et al. 2002). Though, we note that Perez-Becker & Chiang (2013) report that pyroxene is very difficult to remove from even sub-Mercury mass planets in the requisite quantities because of its much lower vapor pressure than olivine.

We consider here, briefly, two different mechanisms for removing mass from KOI-2700b at a rate that is sufficient to produce the hypothesized attenuating dust tail, i.e., $\approx 6 \times 10^9$ g s^{-1}. The first is the generation of a Parker-like wind (Parker 1958) that utilizes the entire bolometric flux of the host star to generate a hydrodynamic outflow. The second is "simple" photoevaporation by heating of the planet's upper atmosphere with XUV radiation (5 Å–912 Å) from the host star.

In the Parker-wind scenario, it appears that there are two major conditions for the generation of dusty comet-like tails on short-period planets. The first was discussed by Rappaport et al. (2012) and suggests that the planet must lie in a favorable equilibrium temperature zone where $T_{\rm eq} \equiv T_{\rm star}\sqrt{R_{\rm star}/a_{\rm orb}}$ is $\gtrsim 2000$ K. Specifically, $T_{\rm eq}$ must be high enough to provide for a molten planet surface (a "lava ocean") with substantial vapor pressures of high-Z materials (i.e., O, Mg, Si, Al, Ca, Fe; see, e.g., Schaefer & Fegley 2009 and Léger et al. 2011) and the generation of an efficient Parker wind to drive material from the planet which then condenses into grains as the vapor cools (Perez-Becker & Chiang 2013). In the type of Parker wind envisioned here, the base of the atmosphere, which is heated by broadband radiation from the host star, drives a hydrodynamic bulk flow of matter which transitions from subsonic to supersonic as it escapes the planet. If conditions are right, this mechanism can drive substantially more mass loss than the Jeans mechanism for atmospheric evaporation (Jeans 1904). Once the dust has formed and is carried away from the planet, $T_{\rm eq}$ cannot be so high that these newly formed and liberated grains rapidly sublimate.

The second condition for a Parker wind, which is at least as important as the first, is the requirement that the planet have a sufficiently low surface gravity (or escape speed) so that it is possible for a hydrodynamic outflow to develop at the atmospheric temperatures typical for close-in planets around K stars (see Rappaport et al. 2012; Perez-Becker & Chiang 2013).

As a crude estimate (explored somewhat further in Rappaport et al. 2012, and in detail in Perez-Becker & Chiang 2013) Parker winds typically operate when the sound speed, c_s, at the base of the atmosphere is ∼5 times lower than the escape speed. For typical heavy molecules that will form grains, the sound speed is $c_s \simeq 1 \times \sqrt{T/2000\,{\rm K}}$ km s^{-1}, while the escape speed from an Earth-size planet is $v_{\rm esc} \simeq \sqrt{2GM_p/R_p} \simeq 10$ km s^{-1}. This fiducial ratio of $v_{\rm esc}/c_s$ is thus ∼10. In order to reduce this by a factor of $\gtrsim 2$ to be more squarely in the Parker-wind regime means decreasing the planet mass by approximately a factor of $\gtrsim 8$ since, at constant density, $v_{\rm esc}$ scales as $M_p^{1/3}$. But, roughly speaking, decreasing an Earth-size rocky planet's mass and radius by factors of $\gtrsim 8$ and $\gtrsim 2$, respectively, puts it in the Mars to Mercury mass and size range. In fact, Perez-Becker & Chiang (2013) find the optimal mass-loss solutions (at least for KIC 1255b) to involve planet masses in the range of 0.01–0.02 $M_\oplus$, corresponding to radii of ∼0.22–0.28 $R_\oplus$, and $v_{\rm esc}/c_s$ as low as ∼2. Thus, if KOI-2700b is indeed a rocky planet that is in the final catastrophic phase of disintegration via dust emission (see Perez-Becker & Chiang 2013), it must be quite small and low in mass.

We now also consider an alternative mass-loss scenario, i.e., that of photoevaporation of the planetary atmosphere driven by the XUV flux from the host star. Following Watson et al. (1981), Lammer et al. (2003), Sanz-Forcada et al. (2011), Lopez et al. (2012), and Kurokawa & Kaltenegger (2013), we write the mass loss rate due to photoevaporation as:

$$\dot{M}_{\rm evap} \simeq \frac{\pi R_p^3 F_{\rm XUV}}{GM_p} = \frac{3F_{\rm XUV}}{4G\rho_p}, \tag{7}$$

where $F_{\rm XUV}$ is the XUV flux at the planet from the host star, and ρ_p is the mean density of the planet. We have neglected the small enhancement term due to the Hill-sphere reduction to the effective potential. Sanz-Forcada et al. (2011) have done a comprehensive job of collecting the X-ray luminosities and inferring the EUV luminosities from several dozen stars of spectral types from K through F. Their Equation (4) summarizes their findings for their entire sample as: $\log(L_{\rm EUV}) \simeq 29.1 - 1.2\log(\tau)$ where τ is the age of the star in Gyr. Since, according to Sanz-Forcada et al. (2011), the EUV flux dominates over the X-ray flux, we take $\log(L_{\rm XUV}) \simeq 29 \pm 1$ (L in erg s^{-1}) for almost any assumption about the age of KOI-2700 (though, according to the Barnes (2007) isochrones, the 11 day rotation period may indicate an age of only ∼250 Myr). Evaluating Equation (7) with plausible parameters for KOI-2700 and KOI-2700b, and a conservatively low range of $\log(L_{\rm XUV}) \simeq 28$–$29$ (erg s^{-1}), we find:

$$\dot{M}_{\rm evap} \simeq 3 \times (10^{10} - 10^{11}) \left(\frac{F_{\rm XUV}}{10^5\,{\rm cgs}}\right) \left(\frac{4{\rm g/cc}}{\rho_p}\right) {\rm g\,s}^{-1}. \tag{8}$$

From an energetics point of view, these values of $\dot{M}_{\rm evap}$ are more than sufficient to eject the requisite rates of mass loss. However, as discussed above, there may be more to producing dusty effluents than simply removing gas molecules. In particular, the gas will likely require the right conditions for it to condense into grains during the outflow, such as might be found in a Parker wind (see Perez-Becker & Chiang 2013). Moreover, the heavier metal molecules, at the same equilibrium ionization temperature of $\sim 10^4$ K, are not moving as rapidly as H, He, or H_2O molecules that may more readily be ejected from a planet. If high XUV fluxes were the only necessary condition for a dust outflow, and low escape speeds were not essential, then there should be numerous other close-in, hot, rocky planets that exhibit dusty tails—which are not, in fact, detected. Using the published distributions of exoplanet transit properties (Burke et al. 2014), one can infer that most hot, rocky planets discovered by *Kepler* exhibit normal transits (see also Sanchis-Ojeda et al. 2014).

In this regard, Kepler-10b and Kepler-78b, with well-studied properties (Batalha et al. 2011; Sanchis-Ojeda et al. 2013; Howard et al. 2013; Pepe et al. 2013), are both short-period ($P_{\rm orb} = 0.83$ and 0.36 days, respectively) rocky planets that do *not* exhibit any evidence for dust emission in their transits. However, their surface gravities are $\sim 2.3\ g_\oplus$ and $\sim 1\ g_\oplus$, respectively, and no Parker-wind is expected to develop in their atmospheres. Hence, this is perfectly consistent with them showing no evidence for dusty emissions in that particular mass-loss scenario.

In keeping with the above considerations, we would *not* expect any "normal-looking" transit, with an inferred rocky planet radius that is $\gtrsim 1/2\ R_\oplus$, to exhibit any hint of a dusty tail. Conversely, if one detects an asymmetric transit, due to a dusty tail, then it will be very difficult to detect the hard body of the planet within the transit unless the host star is quite bright and the photon statistics are extraordinarily high because, by necessity, the planet must be quite small (i.e., $\lesssim 0.3\ R_\oplus$). Moreover, given the complications of the transit shape produced by a dust tail, it may be nearly impossible to detect the hard-body of the planet even with the best of statistics.

Finally, we note that in this work we have not considered models for the asymmetric transit profile other than that caused by a dusty comet-like tail. This is due to the similarities between KOI-2700b and KIC 1255b and the fact that no satisfactory alternative models have thus far been proposed to explain the asymmetric tail in that system. In this regard, we note that the 0.44 day planet PTFO-8-8695b (van Eyken et al. 2012; Barnes et al. 2013) also exhibits some asymmetric transits but with a slow ingress and rapid egress, the opposite of what is seen in KIC 1255b and KOI-2700b. Barnes et al. (2013) attribute the asymmetric transit profiles to a planet whose orbital plane is misaligned with the rapidly rotating host star, thereby leading to transits that are angled across the severely gravity darkened equatorial regions of the star. That scenario, if correct, cannot apply to either KIC 1255b or to KOI-2700b because (1) the rotation periods of those host stars are 20–40 times longer and (2) the transits, including the long egress tails, are substantially longer in duration than the passage of a hard-body planet would be across the disk of either host star. Nonetheless, this object (PTFO-8-8695b) provides at least one example of an asymmetric transit that can be explained without invoking a dust tail.

We thank Eugene Chiang and Josh Winn for helpful discussions. R.S.O. acknowledges NASA support through the Kepler Participating Scientist Program. This research has made use of data collected by the *Kepler* mission, which is funded by the NASA Science Mission directorate. Some of the analysis made use of `PyKE` (Still & Barclay 2012), a software package for the reduction and analysis of *Kepler* data. This open source software project is developed and distributed by the NASA Kepler Guest Observer Office. The *J*-band image of the KOI-2700 field was obtained with the United Kingdom Infrared Telescope (UKIRT) which is operated by the Joint Astronomy Centre on behalf of the Science and Technology Facilities Council of the U.K. Some of the data presented in this paper were obtained from the Mikulski Archive for Space Telescopes (MAST). STScI is operated by the Association of Universities for Research in Astronomy, Inc., under NASA contract NAS5-26555. Support for MAST for non-*HST* data is provided by the NASA Office of Space Science via grant NNX13AC07G and by other grants and contracts.

APPENDIX A

ESTIMATES OF FORCES AND HEATING BY STELLAR WINDS

A.1. Ram Pressure Forces on Dust

For neutral dust particles that are not affected by the magnetic fields entrained in the stellar wind, we consider only the direct ram pressure of the protons and helium atoms colliding with the dust grains. The radial component of the force is given by

$$F_w = \pi a^2\, \mu\, n_w\, v_w^2, \tag{A1}$$

where μ, n_w, and v_w are the mean weight, number density, and velocity of the stellar wind particles, respectively, and a is the radius of a dust grain. The ratio of this force to gravity is given by

$$\beta_w \equiv \frac{F_w}{F_{\rm grav}} = \frac{3\mu v_w^2 n_w d^2}{4GM_s a\rho} \simeq 0.001 \left(\frac{v_w}{200\,{\rm km\,s^{-1}}}\right)^2 \left(\frac{n_w}{10^6\,{\rm cm^{-3}}}\right) \times \left(\frac{d}{5\,R_\odot}\right)^2 \left(\frac{M_\odot}{M_s}\right) \left(\frac{\mu{\rm m}}{a}\right) \left(\frac{4\,{\rm g\,cm^{-3}}}{\rho}\right), \tag{A2}$$

where ρ is the bulk density of the grain material, d is the grain distance from the host star, and we have normalized to plausible parameter values for the stellar wind from KIC 8639908 in the vicinity of KOI-2700b, though these are obviously highly uncertain (see, e.g., Cohen et al. 2011; Bisikalo et al. 2013). We see that the contribution to β from the stellar wind ram pressure, β_w, will be one to two orders of magnitude smaller than due to radiation pressure (see Section 4.2) unless the stellar wind density is extremely and unexpectedly high without the value of v_w also being smaller than 200 km s^{-1}. We note that the implied mass loss rate with these normalization parameters is 2.3×10^{13} g s^{-1}, or about an order of magnitude *higher* than for the Sun. This is plausible for a mid-K star with an angular frequency that is three times higher than that of the Sun.

A.2. Heating of Grains by the Stellar Wind

Under the same set of assumptions as in Appendix A.1 the collisional heating of the dust grains from the stellar wind will be

$$\dot{Q}_w = \frac{1}{2}\pi a^2\, \mu\, n_w\, v_w^3 \simeq 2 \times 10^{-4} \left(\frac{a}{\mu{\rm m}}\right)^2 \times \left(\frac{n_w}{10^6\,{\rm cm^{-3}}}\right) \left(\frac{v_w}{200\,{\rm km\,s^{-1}}}\right)^3 {\rm erg\ s^{-1}}, \tag{A3}$$

where we have normalized to the same estimated parameters as in the previous section. In the absence of heating by radiation, the equilibrium temperature of the dust grains due to collisional heating by the stellar wind would be

$$T_{d,w} \simeq 330 \left(\frac{\epsilon}{0.01}\right)^{-1/4} \left(\frac{n_w}{10^6\,\mathrm{cm}^{-3}}\right)^{1/4} \left(\frac{v_w}{200\,\mathrm{km\,s}^{-1}}\right)^{3/4} \mathrm{K}, \tag{A4}$$

where we have simply taken the emissivity, ϵ, to be grey with an overall value of 1%, independent of particle size or wavelength. Thus, the stellar wind heating would be insignificant compared with radiative heating except in the case of implausibly low emissivities or high stellar wind densities.

APPENDIX B

ORBITAL PARAMETERS FOR THE RELEASED DUST

We start with the assumptions discussed in Section 4.1 for the release of dust particles that are initially nearly at rest with respect to the orbiting planet. The particles suddenly find themselves in an effectively reduced gravity by a factor of $1-\beta$, where β is the ratio of radiation pressure forces to gravity. Start with three basic equations for an arbitrarily eccentric orbit of a test mass around a large central mass, M_s:

$$\text{energy}: \mathcal{E} \equiv -\frac{GM_s(1-\beta)}{2a_d} = -\frac{GM_s(1-2\beta)}{2a_p}, \tag{B1}$$

$$\text{angular momentum}: \mathcal{L}^2 \equiv GM_s(1-\beta)\,a_d\left(1-e_d^2\right) = GM_s a_p, \tag{B2}$$

$$\text{angular frequency}: \omega_d^2 = \frac{GM_s(1-\beta)}{a_d^3}, \tag{B3}$$

where a_d, e_d, $\mathcal{E}$, and $\mathcal{L}$ are the semimajor axis, eccentricity, specific energy, and specific angular momentum of the dust particle, respectively, and the subscript "p" is for the planet. The factor $(1-\beta)$ is introduced to take into account the effective reduction in gravity, or alternatively, the lower effective mass of the host star.

The second equality in the expression for the square of the specific angular momentum is just that of the planet itself, since $\mathcal{L}$ does not change appreciably upon the release of the dust particle. By contrast, the second equality in the expression for the specific energy is modified over that of the planet. This is a consequence of the fact that the specific kinetic energy of the dust is initially the same as that of the planet, while the potential energy is changed due to the reduced effective mass of the host star. A small bit of algebra will show how the term 2β arises.

It is then obvious from the energy equation that

$$a_d = a_p\frac{1-\beta}{1-2\beta}. \tag{B4}$$

If we plug this result for a_d into the angular momentum equation, we can easily solve for the orbital eccentricity of the dust particle:

$$e_d = \frac{\beta}{1-\beta}. \tag{B5}$$

Finally, by combining Equation (B4) with the expression for ω_d, we can express the ratio of dust orbital angular frequency to that of the planet by

$$\left(\frac{\omega_d}{\omega_p}\right)^2 = \frac{(1-2\beta)^3}{(1-\beta)^2}. \tag{B6}$$

The above equations are equivalent to the results given in the set of Equations (2).

We can also provide some insight into the origin of Equation (3) that appears in Section 4.1. Conservation of orbital angular momentum of the dust particle around its orbit requires:

$$\dot{\theta}_d = \frac{\omega_p a_p^2}{r_d^2}, \tag{B7}$$

where the specific angular momentum of the dust is the same as that of the planet, and r_d is the instantaneous radial distance of the dust from the host star at an arbitrary point around the orbit. We then combine this result with the general solution for a Keplerian orbit:

$$r_d = \frac{a_d\left(1-e_d^2\right)}{(1+e_d\cos\theta_d)} \tag{B8}$$

and make use of Equation (B5) to find

$$\dot{\theta}_d = \omega_p\,(1-\beta+\beta\cos\theta_d)^2\,. \tag{B9}$$

From this expression, Equation (3) can readily be derived with just a bit of algebra.

APPENDIX C

APPROXIMATE EXPONENTIAL DECAY OF CROSS SECTION WITH TIME

C.1. Equation of Dust Heating and Cooling

Following Kimura et al. (2002), we write down the equation for determining the equilibrium temperature of dust grains for the assumptions that they (1) are simple spheres, (2) remain at a fixed distance from the parent star, and (3) come into thermal equilibrium on a timescale short compared to their evaporative lifetime.

$$\frac{\pi R_s^2}{d^2}\int_0^\infty \sigma_a(a,\lambda)B(\lambda,T_s)d\lambda = \int_0^\infty 4\pi^2a^2\epsilon(a,\lambda)B(\lambda,T_d)d\lambda, + \mathcal{L}\frac{dm_d}{dt} \tag{C1}$$

where the left-hand side represents the heating of a dust grain at a distance d from the host star, and the two terms on the right-hand side are the radiative cooling of the dust grain and cooling via sublimation, respectively. The subscripts s and d stand for the host star and dust, respectively. The other variables are the absorption cross section, σ_a; the emissivity of the dust grain, ϵ; the latent heat of sublimation, $\mathcal{L}$; and the mass loss rate of the grain, dm_d/dt, which we take to be a positive quantity. By Kirchoff's law, $\epsilon(a,\lambda) = \sigma_a(a,\lambda)/\pi a^2$.

The mass-loss term is

$$\frac{dm_d}{dt} = 4\pi a^2\sqrt{\frac{\mu}{2\pi kT_d}}P_0e^{-\mu\mathcal{L}/k_BT_d}, \tag{C2}$$

where μ is the mean molecular weight and P_0 is the vapor pressure as $T \rightarrow \infty$.

If one considers olivines and pyroxenes, and then plots the left-hand side of Equation (C1) versus the two terms on the right-hand side, individually, it becomes clear that the first term on the right-hand side equals the left-hand side well before the second term on the right-hand side. This indicates that the equilibrium temperature is set by the following much simpler equation:

$$\frac{R_s^2}{d^2}\int_0^\infty \sigma_a(a,\lambda)B(\lambda,T_s)d\lambda \simeq \int_0^\infty 4\sigma_a(a,\lambda)B(\lambda,T_d)d\lambda. \tag{C3}$$

Based on the results of Figure 8 (and similar calculations for other small, but constant, values of *k*; not shown), we find that, to a decent approximation:

$$\sigma_a(a,\lambda) \simeq \text{constant} \times \pi a^2 \left(\frac{2\pi a}{\lambda}\right) \tag{C4}$$

for small particle sizes. The "constant" in this expression depends linearly on the choice of *k*, the complex index of refraction (at least for small values of *k*). Equation (C3) then reduces to:

$$\left(\frac{R_s}{2d}\right)^2 \int_0^\infty \frac{1}{\lambda}B(\lambda,T_s)d\lambda \simeq \int_0^\infty \frac{1}{\lambda}B(\lambda,T_d)d\lambda. \tag{C5}$$

After multiplying and dividing by *T*, the integrals on both sides of the equation become dimensionless and cancel, leaving

$$T_d \simeq \left(\frac{R_s}{2d}\right)^{2/5} T_s \tag{C6}$$

an approximate result that is independent of particle size and composition. If we apply this to KOI-2700, we find $T_d \simeq$ 1650 K.

C.2. Cross Section Decaying With Time

To the extent that the grain temperatures are independent of size, the mass-loss rate, $\dot{m}_d$, given by Equation (C2) implies that $\dot{m}_d$ is simply proportional to the surface area, a^2, for all grains of a given composition (i.e., sharing common values of μ and $\mathcal{L}$). But, for a fixed bulk density ρ

$$\frac{da}{dt} \simeq \frac{\dot{m}_d}{4\pi a^2 \rho} \simeq \mathcal{R}(\mu,\mathcal{L},d,T_s,R_s), \tag{C7}$$

where $\mathcal{R}$ is a "constant" that is understood to depend on the chemical composition of the dust and the properties of, and distance from, the host star.

For small particle scale sizes in the range $0.7 \lesssim 2\pi a/\lambda \lesssim 2$, and for $k \lesssim 0.03$ (the imaginary part of the index of refraction), the extinction cross section (relevant for producing the transit profile) goes like the Rayleigh limit with:

$$\sigma_{\rm ext} \propto \frac{a^6}{\lambda^4} \tag{C8}$$

(see Figure 8). At wavelengths of ∼0.5 to 1 μm, this approximation requires particle sizes in the range of ∼0.06 to 0.3 μm. Thus, the rate of change of the extinction cross section with time, as small particles shrink due to sublimation, is given by

$$\frac{d\sigma_{\rm ext}}{dt} \propto a^5 \dot{a} \propto -a^5 \mathcal{R} \propto -\sigma_{\rm ext}^{5/6} \equiv -\frac{\sigma_{\rm ext}^{5/6}\sigma_0^{1/6}}{\tau}, \tag{C9}$$

where the last expression on the right makes use of two definitions: σ_0 is the cross section before the grain starts to sublimate, and τ is a characteristic decay time which is proportional to the initial size, a_0. Thus, σ_s has the following time dependence:

$$\sigma_{\rm ext} = \sigma_0 \left(1 - \frac{t}{6\tau}\right)^6. \tag{C10}$$

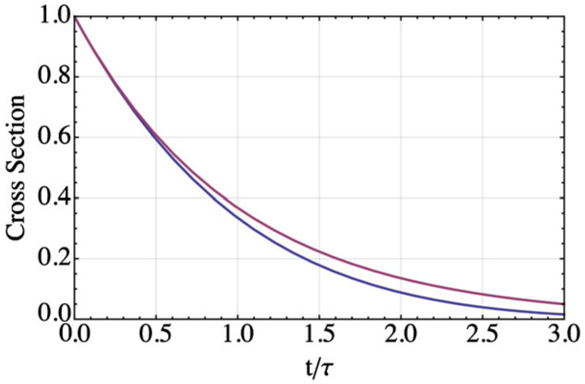

Figure 12. Comparison of the functions $(1 - t/6\tau)^6$ with $e^{-t/\tau}$. The top (red) curve is the exponential.

(A color version of this figure is available in the online journal.)

However, since in the limit of $n \rightarrow \infty$, $(1 - t/n\tau)^n \rightarrow e^{-t/\tau}$, we find that an integer $n = 6$ is sufficiently large to make the exponential solution a decent approximation to the time dependence of the cross section on time. A plot comparing the exponential solution with the $n = 6$ solution is shown in Figure 12. In this expression, the cross section depends sensitively on size, *a*, but the decay timescale, τ, is just linearly dependent on *a*. Thus, if the distribution of grain sizes in the dust tail is limited at the high end by the largest particles that are readily ejected from the planet, and from below by those that decay away quickly, there may be a sufficiently narrow range of particle sizes so that a simple exponential function is a relatively reasonable approximation to the decay of the effective cross section of the particles in the dust tail.

APPENDIX D

ESTIMATE OF MASS LOSS RATE FROM KOI-2700b

As a rough approximation to the geometry of the dust tail, we assume that it is effectively a thin, flat ribbon of thickness Δz in the observer's view direction, with vertical extent Δy in the direction perpendicular to the tail's long direction ($\hat{x}$). Given the rough level of approximation, we further assume that the host star in KOI-2700 presents a uniformly bright stellar disk and that the maximum transit depth therefore occurs just as the planet is on the far side of the disk and just getting ready for its egress. At that moment, the fractional stellar flux that is blocked by a small patch of the tail of area $\Delta y \times dx$ is

$$\frac{\delta F}{F} \simeq \frac{\tau(x)\,\Delta y\, dx}{\pi R_s^2}, \tag{D1}$$

where $\tau(x)$ is the optical thickness, presumed $\ll$1, at location x, y.

The continuity equation allows us to relate the mass loss rate with the dust grain density, $n(x)$, and its flow velocity relative to the planet (see Section 4.1):

$$\dot{M} \simeq \mu n(x)\, v_{\rm rel}(x)\, \Delta z \Delta y, \tag{D2}$$

where μ is the mass of a dust grain before it begins to sublimate, and $v_{\rm rel}(x)$ is the relative velocity of a dust grain as a function of its projected distance x from the planet.

For the relative velocity, we utilize Equation (3) with the approximation that β (the ratio of radiation pressure forces to gravity) is small:

$$v_{\rm rel} \simeq v_{\rm esc} + 4 v_p \beta \sin^2\left(\frac{\theta_d}{2}\right) \simeq v_{\rm esc} + 4 v_p \beta \sin^2\left[\left(\frac{3x}{8\beta d}\right)^{1/3}\right], \tag{D3}$$

where v_p is the orbital velocity of the planet, θ_d is the angular distance traveled by the dust particle in inertial space, and we have added the dust particle's escape velocity from the planet as its approximate initial velocity after escaping (see explanation below). The second form on the right side of Equation (D3) is discussed below. The sinusoidal term in Equation (D3) can be analytically integrated to yield a relation for the offset angle from dust to planet, $\Delta\theta$, under the approximation that, near the dust release point, $\theta_d \simeq \omega_p t$:

$$\Delta\theta \simeq 2\beta(\theta_d - \sin\theta_d) \simeq \frac{1}{3}\,\beta\,\theta_d^3, \tag{D4}$$

where the last equality is for small angles. It is this result that is used to produce the right hand form in Equation (D3) when combined with the small-angle approximation that $\Delta\theta \approx x/d$, where d is the planet's distance from the host star.

The above somewhat ad hoc addition of $v_{\rm esc}$ to Equation (D3) requires a bit of a digression to explain. Initially, the dust moves out roughly spherically symmetrically (perhaps preferentially in the direction of the energy-supplying stellar companion), at roughly the planet's escape speed. After some elapsed time, the radiation pressure induced differential orbital speed between the planet and the dust grows as

$$v_{\rm rel} \simeq 4\, v_p\, \beta\, \sin^2(\omega_p t/2) \tag{D5}$$

until the relative velocity exceeds the magnitude of $v_{\rm esc}$. In the case of KOI-2700, we can use Equation (D5) to find the time for the dust to switch over from a mostly radial outflow to a swept-back comet tail profile, i.e., $v_{\rm rel} \gtrsim v_{\rm esc}$, and this yields 2.5 hr ($\pm 50\%$) for β in the range of 0.02 to 0.07. During this time, the outflow has reached a radial distance from the planet of $\sim 6\ R_\oplus$ ($\pm 50\%$). For the initially expanding cloud, it is straightforward to show, even via a dimensional analysis, that the attenuated starlight is proportional to the radial size of the cloud. And, with a $\sim 6\ R_\oplus$ size, such a cloud cannot make the dominant contribution to the transit or else it would not exhibit such an imposing egress tail. This can also be confirmed after-the-fact from the values of $\dot{M}$ that we infer below. Thus, we utilize a value of $v_{\rm esc}$ as an approximate initial condition for the flow in the comet-shaped tail which we take to start at a distance of $\sim 6\ R_\oplus$ from the planet.

From Equations (D2) and (D3), we can estimate the density of dust along the tail that is attenuating starlight. The optical depth of the dust tail at any point x will be

$$\tau(x) \simeq n(x)\, \Delta z\, \sigma_{\rm ext}\, e^{-x/(\chi R_s)}, \tag{D6}$$

where $\sigma_{\rm ext}$ is the optical extinction cross section (see Figure 8). The exponential factor has been added to take into account the fact that the cross sections of the dust particles are decreasing as the particles sublimate (see Appendix C.2), and χ is a dimensionless scale factor that gives the distance in the tail over which the decay occurs (in units of the stellar radius).

If we combine the above equations, we can write an integral expression for the maximum in the transit depth (assuming an equatorial transit):

$$\frac{\Delta F}{F} \simeq \frac{\dot{M}\sigma_{\rm ext}}{v_{\rm esc}\mu\pi R_s} \int_0^2 \frac{e^{-X/\chi}\, dX}{\left[1 + 4\beta \frac{v_p}{v_{\rm esc}} \sin^2\left(\left\{\frac{3XR_s}{8\beta d}\right\}^{1/3}\right)\right]}, \tag{D7}$$

where $X \equiv x/R_s$.

Finally, we can write an expression for the mass loss rate in terms of the above dimensionless integral which we denote as $\mathcal{I}$:

$$\dot{M} \simeq \frac{\Delta F}{F} \frac{4\,\rho\, a\, v_{\rm esc}\, R_s}{\zeta\, \mathcal{I}}, \tag{D8}$$

where ζ is the extinction cross section in units of πa^2, a is the grain radius, and ρ is the bulk density of the dust material. If we normalize to the parameters appropriate for the KOI-2700 system, we find:

$$\dot{M} \simeq 1.4 \times 10^9 \left(\frac{\rho}{4{\rm g/cc}}\right)\left(\frac{a}{0.3\,\mu{\rm m}}\right)\left(\frac{v_{\rm esc}}{4\ {\rm km\ s^{-1}}}\right)\frac{1}{\mathcal{I}}{\rm g\ s^{-1}}, \tag{D9}$$

where we have taken a fiducial planetary escape speed of 4 km $\mathrm{s^{-1}}$ (2.4–5 km $\mathrm{s^{-1}}$ for the Moon, Mercury, and Mars); $d/R_s = 5.9$ (Table 2), $v_p = 188$ km $\mathrm{s^{-1}}$, and $\zeta = 2$ for dust particles with a dimensionless size parameter of ~ 2 (see Figure 8). The dimensionless integral was done numerically for a range of values of β from 0.01 to 0.1 and a fixed value of $\chi = 2.45$ (inferred from the S parameter in Table 2). The dimensionless integral varies over the range of 0.16–0.58, and we adopt a nominal value of $\mathcal{I} = 0.25$.

The inferred fiducial value of mass loss rate, 6×10^9 g $\mathrm{s^{-1}}$, is equivalent to 0.025 $M_\oplus$ per Gyr, or 2 lunar masses per Gyr.

REFERENCES

Barnes, J. W., van Eyken, J. C., Jackson, B. K., Ciardi, D. R., & Fortney, J. J. 2013, ApJ, 774, 53
Barnes, S. A. 2007, ApJ, 669, 1167
Batalha, N. M., Borucki, W. J., Bryson, S. T., et al. 2011, ApJ, 729, 27
Batalha, N. M., Borucki, W. J., Koch, D. G., et al. 2010, ApJL, 713, L109
Batalha, N. M., Rowe, J. F., Bryson, S. T., et al. 2013, ApJS, 204, 24
Bisikalo, D., Kaygorodov, P., Ionov, D., et al. 2013, ApJ, 764, 19
Bohren, C. F., & Huffman, D. R. 1983, Absorption and Scattering of Light by Small Particles (New York: Wiley)
Borucki, W. J., Koch, D. G., Basri, G., et al. 2011, ApJ, 736, 19
Brogi, M., Keller, C. U., de Juan Ovelar, M., et al. 2012, A&A, 545, 5
Bryson, S. T., Jenkins, J. M., Gilliland, R. L., et al. 2013, PASP, 125, 889
Budaj, J. 2013, A&A, 557, 72
Burke, C. J., Bryson, S. T., Mullally, F., et al. 2014, ApJS, 210, 19
Christiansen, J., Jenkins, J. M., Caldwell, D., et al. 2012, PASP, 124, 1279
Cohen, O., Kashyap, V. L., Drake, J. J., et al. 2011, ApJ, 733, 67
Ford, E. B., & Rasio, F. A. 2006, ApJL, 638, L45
García-Muñoz, A. 2007, P&SS, 55, 1426
Gu, P.-G., Bodenheimer, P. H., & Lin, D. N. C. 2003a, ApJ, 588, 509
Gu, P.-G., Lin, D. N. C., & Bodenheimer, P. H. 2003b, in ASP Conf. Ser. 294, Scientific Frontiers in Research on Extrasolar Planets, ed. D. Deming & S. Seager (San Francisco, CA: ASP), 209
Howard, A. W., Sanchis-Ojeda, R., Marcy, G. W., et al. 2013, Natur, 502, 381
Huang, X., Bakos, G. Á., & Hartman, J. D. 2013, MNRAS, 429, 2001

Jackson, B., Stark, C. C., Adams, E. R., Chambers, J., & Deming, D. 2013, ApJ, 779, 165
Jeans, J. H. 1904, The Dynamical Theory of Gases (Cambridge: Cambridge Univ. Press), 309
Jenkins, J. M., Borucki, W. J., Koch, D. G., et al. 2010, ApJ, 724, 1108
Kawahara, H., Hirano, T., Kurosaki, K., Ito, Y., & Ikoma, M. 2013, ApJL, 776, L6
Kimura, H., Mann, I., Biesecker, D. A., & Jessberger, E. K. 2002, Icar, 159, 529
Kovács, G., Zucker, S., & Mazeh, T. 2002, A&A, 391, 369
Kurokawa, H., & Kaltenegger, L. 2013, MNRAS, 433, 3239
Lammer, H., Selsis, F., Ribas, I., et al. 2003, ApJL, 598, L121
Lecavelier des Etangs, A., et al. 2010, A&A, 514, 72
Léger, A., Grasset, O., Fegley, B., et al. 2011, Icar, 312, 1
Léger, A., Rouan, D., Schneider, J., et al. 2009, A&A, 506, 287
Linsky, J. L., Yang, H., France, K., et al. 2010, ApJ, 717, 1291
Lopez, E. D., Fortney, J. F., & Miller, N. 2012, ApJ, 761, 59
Muirhead, P. S., Johnson, J. A., Apps, K., et al. 2012, ApJ, 747, 144
Murray-Clay, R., Chiang, E., & Murray, N. 2009, ApJ, 693, 23
Ofir, A., & Dreizler, S. 2013, A&A, 555, 58
Parker, E. 1958, ApJ, 128, 664
Pepe, F., Collier Cameron, A., Latham, D., et al. 2013, Natur, 503, 377
Perez-Becker, D., & Chiang, E. 2013, MNRAS, 433, 2294
Pinsonneault, M. H., Deokkeun, A., Molenda-Żakowicz, J., et al. 2012, ApJS, 199, 30
Rappaport, S., Levine, A., Chiang, E., et al. 2012, ApJ, 752, 1
Rappaport, S., Sanchis-Ojeda, R., Rogers, L. A., Levine, A., & Winn, J. A. 2013, ApJ, 773, 15
Rasio, F. A., & Ford, E. B. 1996, Sci, 274, 954
Ruan, S. C., Zhang, F., Zhu, Q., & Zhu, G. P. 2000, Proc. SPIE, 4087, 817R
Sanchis-Ojeda, R., Rappaport, S., Winn, J. N., et al. 2013, ApJ, 774, 54
Sanchis-Ojeda, R., Rappaport, S., Winn, J. N., et al. 2014, ApJ, submitted
Sanz-Forcada, J., Micela, G., Ribas, I., et al. 2011, A&A, 532, A6
Schaefer, L., & Fegley, B., Jr. 2009, ApJL, 703, L113
Schlaufman, K. C., Lin, D. N., & Ida, S. 2010, ApJL, 724, L53
Still, M., & Barclay, T. 2012, Astrophysics Source Code Library, record ascl:1208.004 (http://adsabs.harvard.edu/abs/2012ascl.soft08004S)
van Eyken, J. C., Ciardi, J. R., von Braun, K., et al. 2012, ApJ, 755, 42
Vidal-Madjar, A., Désert, J.-M., Lecavelier des Etangs, A., et al. 2003, Natur, 422, 143
Watson, A. J., Donahue, T. M., & Walker, J. C. G. 1981, Icar, 48, 150
Winn, J. N., Matthews, J. M., Dawson, R. I., et al. 2011, ApJL, 737, L18
Yelle, R. V. 2004, Icar, 167, 30